Spring 2009

# Recent improvements in tensor scale computation and new applications to medical image registration and interpolation

Ziyue Xu
*University of Iowa*

# RECENT IMPROVEMENTS IN TENSOR SCALE COMPUTATION AND NEW APPLICATIONS TO MEDICAL IMAGE REGISTRATION AND INTERPOLATION

by

Ziyue Xu

A thesis submitted in partial fulfillment
of the requirements for the Master of
Science degree in Electrical and Computer Engineering
in the Graduate College of
The University of Iowa

May 2009

Thesis Supervisor: Associate Professor Punam K. Saha

Graduate College
The University of Iowa
Iowa City, Iowa

CERTIFICATE OF APPROVAL

_____

MASTER'S THESIS

_____

This is to certify that the Master's thesis of

Ziyue Xu

has been approved by the Examining Committee
for the thesis requirement for the Master of Science
degree in Electrical and Computer Engineering at the May 2009 graduation.

Thesis Committee: _____
Punam K. Saha, Thesis Supervisor

_____
Milan Sonka

_____
Mona K. Garvin

## ACKNOWLEDGMENTS

First of all, I would like to thank Professor Punam K. Saha for his patient support and guidance for this work. I would also like to thank Professor Milan Sonka for his classes and great support in this work. I sincerely thank Professor Gary E. Christensen and Professor Joseph Reinhardt for all the valuable advice they provided me for my research. Great thanks to Kunlin Cao for her help and friendship. Special thanks to Rong Wang for her support and love. I would also like to thank Professor Mona K. Garvin and other faculties, staffs and students at the Iowa Institute for Biomedical Imaging for their help and lectures.

## ABSTRACT

Tensor scale (t-scale) is a parametric representation of local structure morphology that simultaneously describes its orientation, shape and isotropic scale. At any image location, t-scale is the parametric representation of the largest ellipse (an ellipsoid in 3D) centered at that location and contained in the same homogeneous region.

Recently, we have improved the t-scale computation algorithm by: (1) optimizing digital representations for LoG and DoG kernels for edge detection and (2) ellipse fitting by using minimization of both algebraic and geometric distance errors. Also, t-scale has been applied to computing the deformation vector field with applications to medical image registration. Currently, the method is implemented in two-dimension (2D) and the deformation vector field is directly computed from t-scale-derived normal vectors at matching locations in two images to be registered. Also, the method has been used to develop a simple algorithm for computing 2D warping from one shape onto another. Meanwhile, t-scale has been applied to generating interpolation lines with applications to medical image interpolation using normal vector. Normal vector yields local structure orientation pointing to the closest edge. However, this information is less reliable along the medial axis of a shape as it may be associated with either of the two opposite edges of the local shape. This problem is overcome using a shape-linearity measure estimating relative changes in scale along the orthogonal direction. Preliminary results demonstrate the method's potential in estimating deformation between two images and interpolating between neighboring slices in a grey scale image.

## TABLE OF CONTENTS


LIST OF TABLES ..... v

LIST OF FIGURES ..... vi

CHAPTER ONE INTRODUCTION ..... 1

1.1 Tensor Scale ..... 1
1.2 Non-rigid Registration ..... 3
1.3 Medical Image Interpolation ..... 4
1.4 Outline ..... 6

CHAPTER TWO METHODS ..... 8

2.1 Tensor Scale Computation ..... 8
2.1.1 General Procedure ..... 8
2.1.2 Intensity Computation ..... 9
2.1.3 Edge Location ..... 10
2.1.4 Edge Repositioning ..... 13
2.1.5 Ellipse Fitting ..... 14
2.1.6 T-Scale Computation Result ..... 16
2.2 T-scale Based Registration ..... 17
2.2.1 Introduction to Image Registration ..... 17
2.2.2 T-scale Based Registration ..... 17
2.2.3 Image Warping ..... 20
2.3 T-scale Based Interpolation ..... 21
2.3.1 Premise Analysis ..... 21
2.3.2 Interpolation Method ..... 22
2.3.3 Local Scale and Medial Region Problem ..... 23
2.3.4 Performance Evaluation ..... 26

CHAPTER THREE RESULTS ..... 27

3.1 T-scale based Registration ..... 27
3.1.1 Applications to Image Warping for Geometric Shapes ..... 27
3.1.2 Applications to 2D registration of CT images ..... 29
3.2 T-scale based Interpolation ..... 31
3.2.1 Data and Method Description ..... 31
3.2.2 Result on Phantom Data ..... 33
3.2.3 Result on Real Image ..... 37

CHAPTER FOUR DISCUSSION ..... 39

CHAPTER FIVE CONCLUSION ..... 40

APPENDIX A SAMPLE SLICES FOR ROBUSTNESS TEST ..... 41

APPENDIX B SLICE-BY-SLICE RESUTL FOR REAL DATA ..... 43

APPENDIX C SAMPLE SLICES FOR REAL DATA ..... 44

REFERENCES ..... 45

## LIST OF TABLES

Table 1 Mean absolute errors (gray value range 0~255) and standard deviation of the absolute errors between 20 pairs of successive image slices before and after applying different registration methods.....30

Table 2 Paired t-test result for slice-by-slice performance analysis .....34

## LIST OF FIGURES

Figure 1 Illustration of different steps in computation of t-scale at a point. ..... 9

Figure 2 Illustration of different types of errors during discretization of the Laplacian of Gaussian function. ..... 11

Figure 3 Illustration of error values with different sample periods during discretization of the Laplacian of Gaussian function ..... 13

Figure 4 Results of ellipse fitting using the geometric distance approach result with different initializations. ..... 15

Figure 5 Results of t-scale computation on a sagittal image slice from an MR brain image. ..... 16

Figure 6 Applying normal vector in deformation field computation. ..... 18

Figure 7 Different t-scale features used for image registration. ..... 19

Figure 8 Illustration of computing the interpolation line. ..... 22

Figure 9 Local scale derived from t-scale used for image interpolation ..... 24

Figure 10 Illustration of correcting false coupled normal vectors near medial axis of a structure using local scale. ..... 25

Figure 11 Illustration of warping a disk onto a square. ..... 28

Figure 12 Illustrations of different shapes during deformation of a Y-like target shape onto a disk via an intermediate shape. ..... 28

Figure 13 Results of application of t-scale based image registration on two successive image slices from CT data set of a cadaveric ankle specimen. ..... 30

Figure 14 Performance of different interpolation methods on BrainWeb data at difference slices measured by MAD. ..... 33

Figure 15 Performance of different interpolation methods on BrainWeb data at difference slices measured by square root of MSD. ..... 34

Figure 16 Performance of different methods for data at different noise level measured by (a) MAD and (b) square root of MSD. ..... 35

Figure 17 Performance of different methods for data at different level of intensity non-uniformity measured by (a) MAD and (b) square root of MSD. ..... 36

Figure 18 Performance of different methods on 12 images measured by (a) MAD and (b) square root of MSD. ..... 37

Figure A1 Phantom image for different level of intensity non-uniformity. ..... 41

Figure A2 Phantom image for different noise level ..... 42

Figure B1 Slice-by-slice result of square root of mean square difference generated by 3 interpolation methods for lung CT data. ..... 43

Figure C1 One sample slice from lung CT data with the result given by 3 different interpolation methods. ..... 44

# CHAPTER ONE

# INTRODUCTION

## 1.1 Tensor Scale

Scale [1-4] plays an important role in many medical imaging applications and is useful in determining the optimum trade-off between noise smoothing and perception/detection of structures. It may be thought of as the spatial resolution, or, more generally, a range of resolutions needed to ensure a sufficient yet compact object representation [1]. Witkin [2] and Koenderink [3] mathematically formulated the concept of scale in the form of scale-space theory. Discrete scale-space representations [4] have been used in several imaging applications including segmentation [5], clustering [6], classification [7], and structural analysis [8]. The notion of "local scale" [9-12] emerged from the needs of spatially tuning neighborhood kernel size [13] or developing space-variant parameter controlling strategies [14] toward improving the performance of different methods. Local structure-based morphometric scale information may be useful to several applications such as filtering, edge detection, object segmentation, registration, analysis of regional structural properties including orientation, thickness, shape, etc. We refer to this notion of scale as "local morphometric scale" and briefly "local scale".

Saha et al. [13, 14] initiated the notion of local morphometric scale using a spherical model that was applied to image segmentation [13, 15, 16], filtering [14], registration [17], and removal of partial volume effects in rendering [18]. Although our preliminary results have demonstrated effectiveness of this notion of local scale in different image processing applications, a major limitation of the spherical model is that it ignores orientation and anisotropy of local structures. For example, the spherical model

of local scale would not be efficient in smoothing along a narrow elongated structure. Also, spherical scale would not be able to classify trabeculae in a trabecular bone network as belonging to plates and rods nor to identify their orientations. These limitations of spherical or isotropic model of local scale led to the notion of "tensor scale" – a local morphometric parameter yielding a unified representation of structure size, orientation, and anisotropy [19, 20]. Tensor scale is a valuable feature associated with every image point and is potentially useful in several image processing and computer vision applications, especially the medical imaging applications where local structural and scale information may play important roles. A few works have been reported on representing local orientation using gradient structure tensor [21-25]. Recently, Weijer et al. [24] and Rieger and van Vliet [25] have proposed new methods to estimate curvature of space curves using gradient tensor field. Although, gradient tensor field efficiently provides orientation information near edges, it may not yield shape and size or thickness information, especially, at locations far away from edges. Recently, a generalized local scale concept [26] has been developed where the local scale at a point is represented as the largest set of points connected to the candidate point under a homogeneity criterion.

Saha et al. [19, 20] described tensor scale at an image location as the parametric representation of the largest ellipse (or, ellipsoid in three-dimensions) centered at that image location and contained inside the same homogeneous region under a predefined criterion. They have presented a computational solution [20] to compute tensor scale in grey level images and investigated the effectiveness of the new local morphometric scale in image segmentation [27], registration [28], filtering [20] and also in quantifying local morphometry in complex quasi random network of plates and rods in human trabecular

bone via in vivo imaging [29, 30]. Recently, Andalo et al. introduced a new shape descriptor based on tensor scale [31] and used it in detection of salience on a given contour [32].

Although, the computational framework proposed by Saha et al. is robust and effective, optimization of several steps were not studied. One major contribution of this paper is to optimize the steps needed for tensor scale computation. Specifically, we optimized digital LoG and DoG kernels for edge detection at varying kernel size and ellipse fitting algorithm by using minimization of both algebraic and geometric distance errors.

### 1.2 Non-rigid Registration

We investigate the potential role of tensor scale in non-rigid image registration and the preliminary results are presented.

Image registration computes the transformation that optimally maps one image onto another under certain matching criterion. Properties of such transformation function may vary from rigid body to free-form transformations depending upon the application and experimental setup. Many medical imaging applications [33-35] demands free form registration of anatomic structures in different images which may be caused by – (1) physiologic motion, (2) changes in size and shape due to disease or natural growth and (3) shape and size variations across subjects. Research interests on deformable image registration have grown not only for its paramount importance in medical imaging but also due to the immense challenges and difficulties it poses. An accurate and reliable solution to this problem will highly aid research studies involving cross-modality and

population and atlas-based analysis and temporal analysis for monitoring a treatment or disease progression.

Many deformable registration approaches have been proposed in literature [36-41]. A deformable registration algorithm primarily deals with the following three challenges – (1) an efficient similarity measure, (2) an effective spatial transformation model and (3) a transformation control and optimization strategy. A solution to the last two challenges leads to a basic registration framework [37, 39-41] and somewhat less dependent on the research relating the first challenges[36, 38]. The similarity measure controls the changes in the deformation function in its parametric space. Roles of several similarity measures, including landmarks [36], intensity [37], mutual information [38] or joint entropy [42], have been studied in the context of deformable registration. The spatial transformation model and control strategy defines the relationship between regions in two images and enforces topological consistency of registration. Several transformation models have been popularly adopted in literature including elastic model [39], viscous fluid model [40, 41] and optical flow [37]. Generally speaking, an image is modeled as a physical deformable body where measures of similarity contribute to the "external force" while the spatial transformation model constitutes the "internal force", and the overall goal of registration is finding the equilibrium of deformation at minimal energy.

### 1.3 Medical Image Interpolation

We developed a tensor scale based image interpolation method and tested its potential by comparing its preliminary result on both phantom and real data sets with registration based method.

Medical images are often represented as a set of slices. As a three-dimensional data set, distances between voxels are important parameters that determine the isotropic character of the data set. The thickness of each slice is often greater than the distance between two neighboring pixels within a slice. Therefore, most raw data set of medical imaging is composed of voxels that are anisotropic. However, isotropic or near isotropic 3D data is desirable in a number of image processing, analysis and visualization tasks. Therefore, interpolation, which is used as a preprocessing step, is often performed to increase the resolution perpendicular to the slice planes to restore the isotropy of the data set before applying any visualization or analysis techniques.

For this type of inter-slice interpolation problem, there are mainly two kinds of techniques: scene-based and object-based methods [43]. Scene-based interpolating approaches are based only on the image intensities and voxel location within the image. This group includes well-known methods such as nearest neighbor, linear, spline, and kernel-based interpolation [44] which is a complex enhancement for the former methods. Scene-based techniques are easier to implement, but significant artifacts could be generated during this process because in practical applications, anatomical structures always shift considerably between slices, which inevitably breaks the priori assumption in such methods that in estimation, pixels used in the original slices belong to the same anatomic structure.

Object-based interpolation techniques extract additional information from the image slices to guide the process to get more accurate result as pixels belonging to the same anatomic structures on the different slices can be determined and grouped. The interpolation can then be performed within structures. Many methods are proposed in this

category, for example, shape-based methods [45, 46], registration-based methods [47] and morphology-based methods [48]. These techniques provide a practical way to interpolate between segmented slices. However, some of these methods only interpolate binary images, and some involve a preliminary intensity-based registration between slices to judge corresponding positions.

### 1.4 Outline

In this paper, we improve the t-scale computation algorithm by – (1) optimizing digital LoG and DoG kernels for edge detection at varying kernel sizes and (2) ellipse fitting by using minimization of both algebraic and geometric distance errors. Also, we have applied t-scale for 2D image registration, warping and interpolation and have presented preliminary results. Toward this goal, we have developed a new method based on "normal vector". Given the computed t-scale at an image point, the nearest edge binding the local structure can be defined and the normal vector is computed by the vector joining the point and the nearest binding edge. This normal vector may vary over the entire 360° angular space unlike the original t-scale orientation which varies only over 180°. Normal vector is a useful image feature representing a high level local morphological property in an image and may be directly computed from a gray level image requiring no image segmentation.

In Chapter 2, we present the improved t-scale computation algorithm followed by a new t-scale based 2D image registration method and a t-scale based medical image interpolation method.

In Chapter 3, the results of application of the t-scale based registration and interpolation method on both phantom and real images are presented and compared with other methods of BSpline based registration and registration based interpolation.

In Chapter 4, we discuss some problems encountered and explore future extensions.

In Chapter 5, the work of this thesis is summarized.

# CHAPTER TWO

# METHODS

In this section, we present the improved t-scale computation algorithm with optimized edge detection and ellipse fitting. It is followed by the description of the new t-scale-based two-dimensional registration method and interpolation method.

## 2.1 Tensor Scale Computation

### 2.1.1 General Procedure

T-scale is computed by locating the edge points visible from a given point $p$ along different directions which are then used to compute the t-scale ellipse at $p$. The basic steps in tensor scale computation are as shown in Figure 1:

1) Generate a set of radially opposite sample line pairs with the candidate point as origin (red) and compute the intensity along these sample lines.
2) Trace the closest edge point on each sample line (blue and yellow).
3) Reposition the edge locations (yellow) so that the two edges on a pair of sample lines are equidistant to the candidate point (green) satisfying axial symmetry.
4) Determine the t-scale by computing the best fit ellipse to the repositioned edge points.

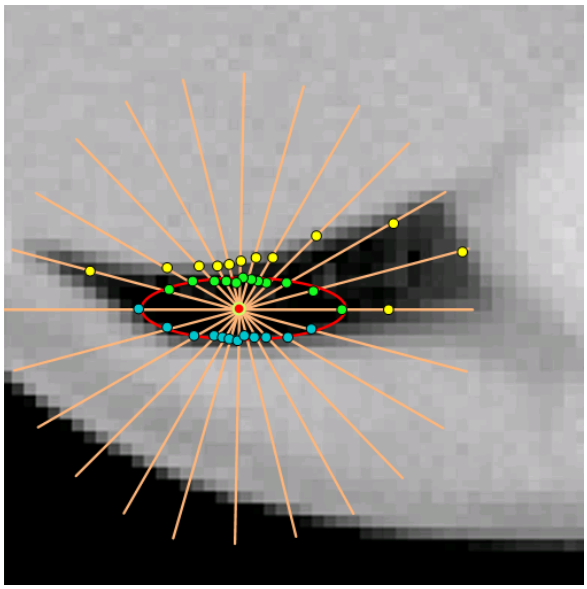

Figure 1 Illustration of different steps in computation of t-scale at a point (red). The method starts with edge location (blue and yellow) on sample lines emanating from the candidate point. Following axial symmetry of an ellipse, the edge points on each pair of radially opposite sample lines are repositioned (yellow to green). Finally, tensor scale ellipse (red) is computed from repositioned edge points.

Edge detection and ellipse fitting are the two critical steps in t-scale computation framework that largely determine the overall performance and accuracy of the method. Noise and blurring can often cause errors in edge detection leading to artifacts in local structural definition captured in t-scale. With the ellipse fitting step, the primary object is the synergy between accuracy and computational complexity. In the following, we briefly discuss each of the above steps and describe the improvements achieved here.

### 2.1.2 Intensity Computation

We select $m$ pairs of mutually opposite sample lines at an approximately uniform distribution over the entire angular space ensuring that the final tensor scale is not skewed

in any direction. Two parameters are identified with sample lines, namely, the sampling interval and the length of each sample line. The length $L$ of a sample line represents the largest distinguishable local scale/structure size; i.e., it limits the extent of locality or neighborhood size. Such parameter should be carefully chosen. Obviously, too small value of sample line length is not desirable; again a very large value of this parameter adds to the computational burden while the additional information may not be so important. Therefore, a correct choice of the sample line length parameter is important and application dependent. The sample interval $\delta$ determines the density of sample points on a sample line and a right choice of $\delta$ are determined by the trade-off between the computational complexity and the scale of the finest detectable structure. Assuming that the image resolution is synchronized with the target application, we recommend choosing $\delta$ between 1 and 0.5 times the smallest dimension of a voxel. The intensity at any sample points is determined using linear interpolation of the four binding grid points. Let $f_i^p(v)$ denote the intensity computed at the $v^{th}$ sample point on the $i^{th}$ sample line emanating from the pixel $p$.

### 2.1.3 Edge Location

To eliminate the effects of locally disconnected structures of similar intensities during edge detection, two intensity connections $\mu_{UP}$ and $\mu_{DN}$ are derived from the intensity values $f_i^p(v)|v = 0,1,2,\ldots$ before applying edge detection on the $i^{th}$ sample line emanating from $p$

$$\mu_{UP}(v) = \max_{x=0,1,\cdots v} f(x), \quad \mu_{DN}(v) = \min_{x=0,1,\cdots v} f(x).$$

The above two connected intensity profiles along a sample line significantly eliminate the effects of locally disconnected structures intersecting with the sample line without causing any blurring and thus preserving thin structures. These two intensity connections are used to separately handle the cases of "step-up" and "step-down" edges.

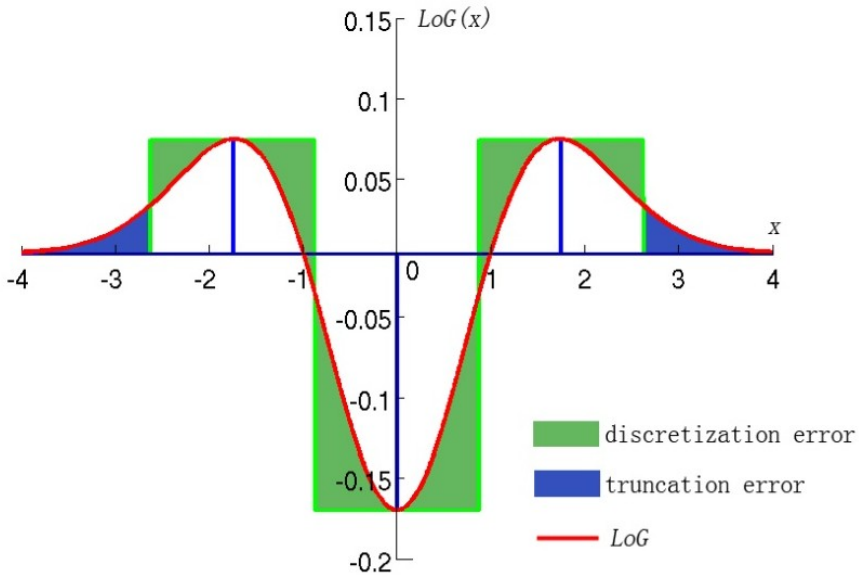


Figure 2 Illustration of different types of errors during discretization of the Laplacian of Gaussian function generating a discrete LoG kernel of size $2 \times 1 + 1$.

Conventional LoG and DoG [49] are used for detecting edges on the one dimensional (1D) intensity profile along each sample line. An edge is located at the first zero crossing of the LoG with the strength of intensity gradient computed as DoG, exceeding a threshold. One of the most critical issue here is to determine discrete kernels for LoG and DoG under a given computational constrain. Specifically, we have developed an optimization method to compute the discrete kernels for LoG and DoG for a given kernel width. In the following, we describe the kernel optimization method.

Optimizing a discrete kernel representing LoG or DoG is an important and useful problem. Gunn [50] have reported a task- and image-dependent approach for optimizing a discrete kernel for LoG. However, a kernel optimized for one type of image may not optimally perform on another image. Here, we adopt a task- and image-independent approach of optimizing discrete LoG and DoG kernels. Essentially, our method is based on minimizing discretization errors under the constraint of a given kernel length. As illustrated in Figure 2, discretization of the continuous LoG involves two types of errors and we refer to these errors as discretization and truncation errors. Let $LoG(x)$: $R \rightarrow R$ denote the continuous LoG function while $dLoG[n]$: $\{-N, \cdots, 0, \cdots, N\} \rightarrow R$ denote the discrete LoG kernel for a given kernel size. Let $\delta$ denote the sample period of the LoG kernel. It can be noticed from Figure 3 that the discretization error increases with $\delta$ while the truncation error decreases with it. The discrete LoG kernel without scaling is to determine the $\delta$ minimizing the total errors. For a given $\delta$, *dsLoG*[$n$] is determined as the average LoG value over the interval $n\delta - \delta/2 \leq x < n\delta + \delta/2$. A scaling factor is needed due to the fact that, while the integral of the continuous LoG function over its domain is always zero, the same may not be claimed for the discrete kernel $dsLoG$ without scaling. This discrepancy may lead to an artifactual shift in computing zero crossing. This problem is overcome by scaling the discrete kernel as following:

$$dLoG[n] = \begin{cases} \frac{1}{s} \times dsLoG[n], & dsLoG[n] \geq 0 \\ s \times dsLoG[n], & dsLoG[n] < 0 \end{cases}$$

where $s$ is the ratio of the sum of positive $dsLoG$ values to that of negative values. Finally, the value of $\delta$ is determined that minimizes the total error. Profiles of different

types of errors during discretization of the Laplacian of Gaussian function generating a discrete LoG kernel of size $2 \times 1 + 1$ is illustrated in Figure 3.

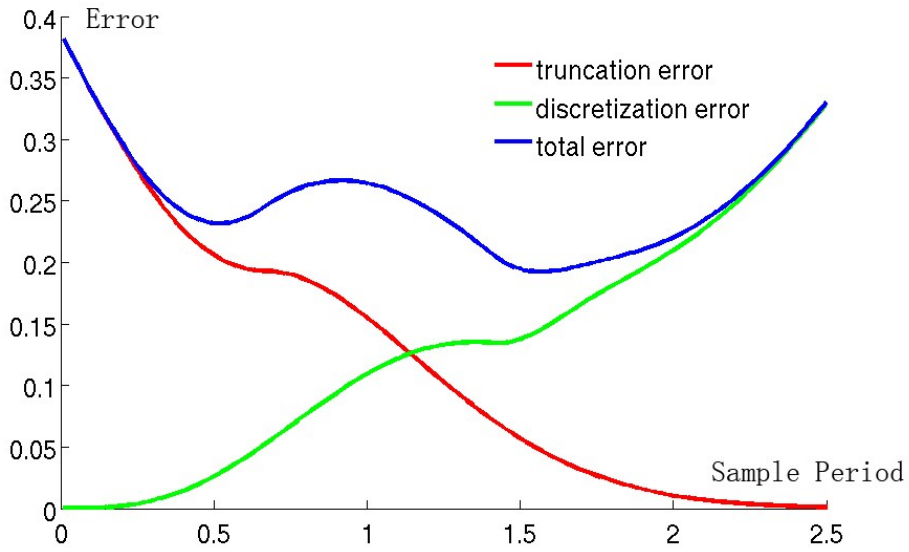


Figure 3 Illustration of error values with different sample periods during discretization of the Laplacian of Gaussian function generating a discrete LoG kernel of size $2 \times 1 + 1$.

### 2.1.4 Edge Repositioning

The edge points obtained in the previous step are intended to roughly describe the boundary of the t-scale ellipse centered at the candidate point $p$. Following the axial symmetry of an ellipse, for each pair of opposite sample lines, the two edge points should be equidistant from $p$ which is the center of the t-scale ellipse. However, the detected edge points on a local structure generally do not satisfy this symmetry. For example, in Figure 1, the edge locations colored yellow on the north-bound sample lines are mostly farther from the edges on corresponding opposite sample lines. Therefore, the edge points need to be repositioned by analyzing the edge points on every pair of sample lines.

Specifically, between the two edge points on a pair of sample lines, the one closer to the candidate point $p$ is selected and reflected on its complementary sample line. The edge locations colored green are obtained using this repositioning algorithm.

### 2.1.5 Ellipse Fitting

As discussed before, the last step in tensor scale computation is to fit an ellipse to the edge points. In our application, the number of edge points is significantly larger as compared to the number of parameters needed to represent an ellipse. The literature on ellipse fitting is quite matured and there are several established approaches available in the literatures [51-53] to accomplish the job. All ellipse fitting approaches essentially minimize the error between the observed data (here, the edge points) and the computed ellipse. Primarily, these methods differ with respect to the nature of these errors. Here, we have investigated two different kinds of distances defining errors, namely, algebraic and geometric distances. When errors are defined using algebraic distance, a canonical solution can be derived leading to a computational efficient solution. However, the solution may not be stable for highly anisotropic data sets. In our application, such situations may occur frequently, especially, when a candidate point is close to an edge. Geometric distance approach generates stable solutions for most ellipses and also uses more natural Euclidean distance metric. Unfortunately, it is difficult to derive a canonical form of solution for ellipse fitting optimizing geometric distance error, and therefore, a geometric distance based approach is commonly realized using an optimization technique raising issues relating to initialization. Here, we use the algebraic distance based solution for initialization to the geometric distance based approach providing that the former method yields a real ellipse. Under the situation where algebraic distance fails, principal

component analysis of repositioned edge points is used to obtain the initial solution. The entire ellipse fitting algorithm is summarized in the following:

*Step 1:* Translate all $r$ edge points so that the candidate point $p$ is moved to the origin.

*Step 2:* Compute the covariance matrix of the translated $r$ edge points and compute its eigenvectors $\mathbf{i}_1$ and $\mathbf{i}_2$ and the eigenvalues $\lambda_1$ and $\lambda_2$.

*Step 3:* Rotate the $r$ edge points around the origin so that $\mathbf{i}_1$ and $\mathbf{i}_2$ are aligned to the coordinate axis. Solve the canonical equations for algebraic distance approach to compute the ellipse.

*Step 4:* If the ellipse computation in Step 3 is real, use it for Step 5. Otherwise, use the ellipse with semi axis $\lambda_1\mathbf{i}_1$ and $\lambda_2\mathbf{i}_2$ for Step 5.

*Step 5:* Compute the final ellipse by minimizing total geometric distance error from $r$ edge points with the initialization obtained in the previous step. Newton's algorithm along with the Jacobian of the error function is iteratively used to obtain the optimization of the target ellipse.

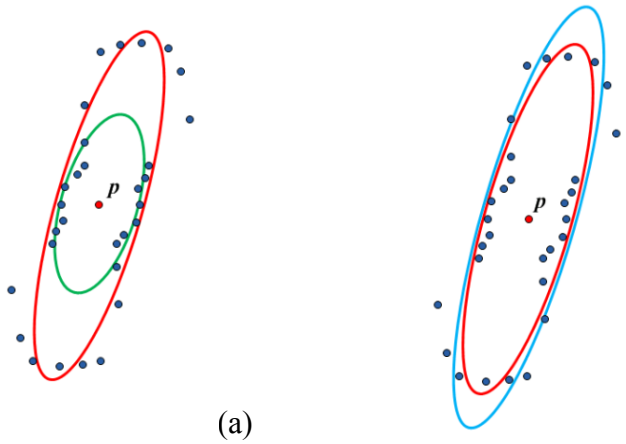


Figure 4 Results of ellipse fitting using the geometric distance approach result (red) with different initializations. (a): using principal component analysis (green) and (b): optimizing algebraic distance error (blue).

Figure 4 illustrates the final ellipse fitting with both PCA and algebraic distance based initialization. It can be noticed that both initialization lead to very similar ellipses.

### 2.1.6 T-Scale Computation Result

To display a tensor scale image, we apply a HSI color coding scheme following the fact that an ellipse centered at origin is uniquely defined by three factors - orientation of the major semi axis $\theta$, anisotropy $\sqrt{1-b^2/a^2}$, and thickness $b$. We scale all three parameters to the regular range of hue, saturation and intensity and assign the values of these three parameters to HSI respectively. Thus, hue component represents orientation, saturation component represents how close the ellipse is to a circle and intensity represents the t-scale thickness of local structures as shown in Figure 5.

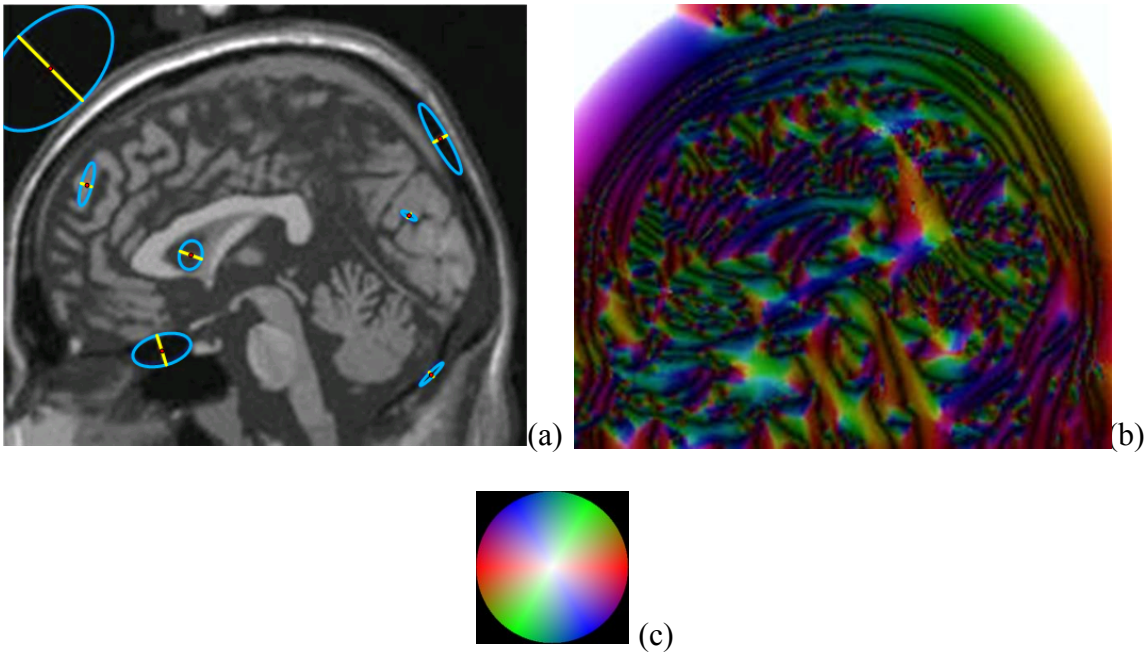


Figure 5 Results of t-scale computation on a sagittal image slice from an MR brain image. (a) An original image with computed t-scale ellipses illustrated at a few locations. (b) Color coded display of t-scale image using an HSI color coding shown in (c).

## 2.2 T-scale Based Registration

### 2.2.1 Introduction to Image Registration

Image registration has many uses in medical applications such as atlas based image segmentation, motion modeling, and multi-modality fusion. The fundamental assumption in these applications is that a correspondence mapping between anatomical images can be defined by image registration. Specifically, for deformable registration method, the primary objective is to compute a deformation vector field that warps a target image onto a reference image. In other words, for each point in the target image, we need to determine its correspondence in the reference image.

### 2.2.2 T-scale Based Registration

Here, we describe a direct method of computing this deformation vector field using t-scale. The principle of the t-scale-based deformation field computation method is illustrated in Figure 6. The underlying idea behind the method is to first use t-scale at a point to determine its associated local structure boundary and then compute local deformation vector by analyzing the movement of local structure boundaries in the images. As illustrated in Figure 6 (a), it is not obvious from the t-scale of $a$ as whether $b$ or $c$ is the local structure boundary of $a$. However, we can easily solve this confusion by analyzing t-scale thickness of the points along the minor axis of the t-scale at $a$. Obviously, t-scale thickness of points decreases along $\overrightarrow{ab}$ from $a$ to $b$ and increases along $\overrightarrow{ac}$ from $a$ to $c$. We refer to the vector $\overrightarrow{ab}$ as normal vector of $a$. A color coded display of normal vector map for the phantom image of Figure 7 (a) is illustrated in Figure 7 (c). Let $\boldsymbol{\tau}_t(a)$ denote the normal vector in the target image at a pixel location a and let $\boldsymbol{\tau}_r(a)$

denote the same in the reference image. Following the drawing of Figure 6 (b), $\boldsymbol{\tau}_t(a) = \overrightarrow{ab}$, and $\boldsymbol{\tau}_r(a) = \overrightarrow{ac}$. Assuming that the point $b$ in the target image corresponds to the point $c$ in the reference image, the deformation vector at a is defined as $\boldsymbol{\tau}_r(a) - \boldsymbol{\tau}_t(a) = \overrightarrow{ac} - \overrightarrow{ab} = \overrightarrow{bc}$. Then the point $a$ of the target image should be deformed at $a'$ in the reference image.

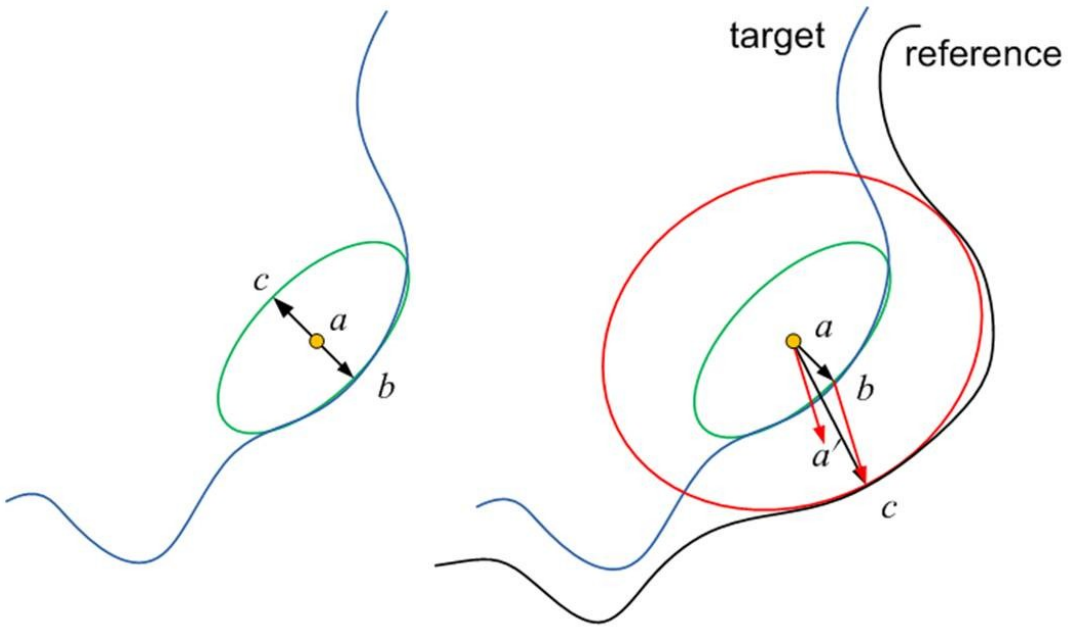


(a) (b)

Figure 6 Applying normal vector in deformation field computation. (a) Description of the normal vector derived from t-scale. (b) Illustration of computing the deformation vector at an image point $a$ with the information from target and reference images.

A major challenge with this approach is that the normal vector is unstable near the medial axis of a local structure. The normal vector along the medial axis may associate with either of the two opposite boundaries of the local structure which is a significant

source of errors in our method. This problem is solved using the observation that the change in t-scale thickness across the structure is nonlinear near medial axis and we refer to this measure as scale-linearity (see Figure 7 (e)). Specifically, scale-linearity $\gamma(p)$ at any point $p$ is determined as follows:

$$\gamma(p) = \frac{1}{2}\left(\left|\boldsymbol{\tau}\left(p + \frac{\boldsymbol{\tau}(p)}{|\boldsymbol{\tau}(p)|}\right)\right| - \left|\boldsymbol{\tau}\left(p - \frac{\boldsymbol{\tau}(p)}{|\boldsymbol{\tau}(p)|}\right)\right|\right)$$

This linearity measure is used as a weight while filtering the deformation field to generate a smooth deformation vector field.

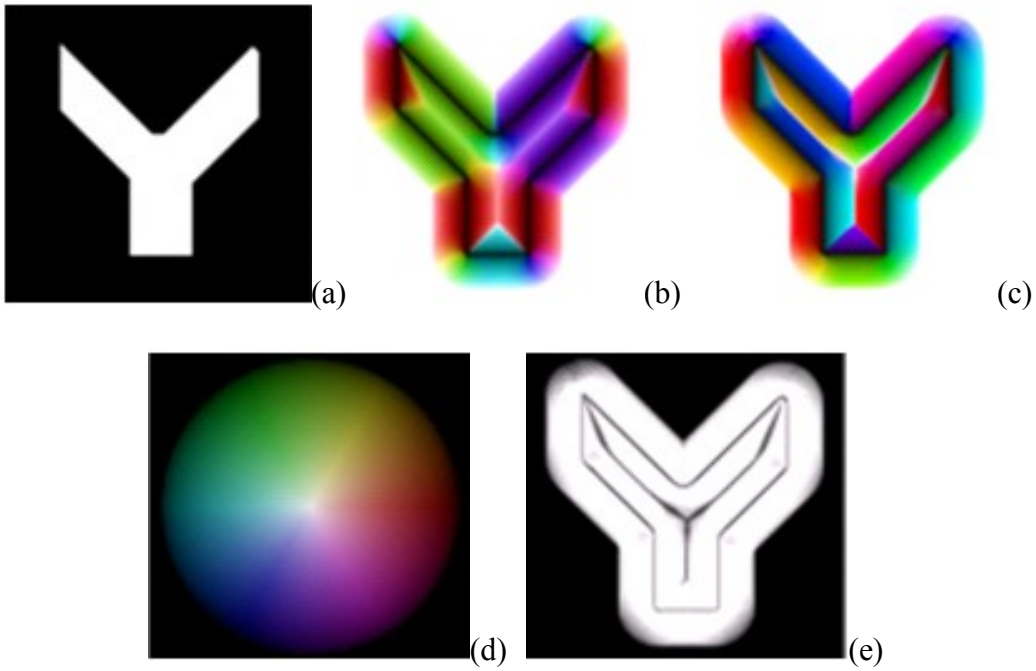


Figure 7 Different t-scale features used for image registration. (a) A binary phantom image. (b) T-scale image displayed using the color coding of Figure 5 (c). (c) Display of the normal vector map using the color coding of (d) uniquely describing the entire 360° angular space. (e) Linearity map with sharp change in intensity around medial axes.

### 2.2.3 Image Warping

For non-rigid image registration, a point $a$ in reference image $R$ is mapped to point $b$ in target image $T$ with deformation $h(x) = x + u(x)$ such that $b = h(a)$. One important issue during this warping process is to preserve topology, or in other words, the resulting deformation field needs to be smooth. Different methods apply various techniques to ensure this requirement. For example, methods based on optical flow [37] apply a Gaussian convolution filter to the deformation field during the end of each iteration to regularize the deformation field; while methods based on continuum mechanics [54] iteratively estimate the transformations and restrict them to preserve topology by adding regularization constraint to the cost function. The constraint is derived from continuum mechanics such as linear elasticity and viscous fluid.

In our algorithm, the deformation field computed using t-scale cannot guarantee its smoothness by computation procedure itself. So instead of warping the reference image using the full deformation field computed directly from t-scale, a "force field" acted on $R$ at point $a$ is generated as

$$\boldsymbol{f}(a) = k[\boldsymbol{\tau}_{\mathrm{r}}(a) - \boldsymbol{\tau}_{\mathrm{t}}(a)]$$

where $k$ denotes a small constant defining the magnitude relationship between the force and the full deformation. Further, a similar process as the "demons" method [37] is adopted, using Gaussian filtering that smoothes the force field to get the deformation field at each iteration. The only difference is that a linearity weighted Gaussian filtering is applied to overcome the medial axis problem. Let $\Omega$ be the region centered at candidate point $a = (i_0, j_0)$ and defined by the Gaussian kernel $G(i,j) = e^{-(i^2+j^2)/2\sigma^2}, -t \le i \le t, -t \le j \le t$, the weighted (with weight $W(i,j)$) Gaussian filtering result is

$$\overline{\boldsymbol{f}(a)} = \frac{\sum_{(i,j)\in\Omega} G(i,j) \cdot W(i,j) \cdot \boldsymbol{f}(i,j)}{\sum_{(i,j)\in\Omega} G(i,j) \cdot W(i,j)}$$

Note that the kernel size varies according to the total weight so that the kernel won't lie completely in the "bad region". Current implementation uses constant force and control the warping process by selecting the number of iterations, as well as monitoring the mean absolute error between the target image and the warped result.

## 2.3 T-scale Based Interpolation

### 2.3.1 Premise Analysis

T-scale based interpolation relies on the assumption that adjacent slices contain similar anatomical features, and that t-scale at the same coordinate of the two slices is capable of mapping these similar features together. Thus the displacement of a structure between two adjacent slices should not be greater than half the structure size. If this assumption is violated, and an anatomical feature shifts out of the capabilities of tensor scale algorithm from one slice to the next, then the advantages of tensor scale based approach will be lost.

Under such assumption, t-scale based interpolation can be designed following a different manner from the warping strategy applied for image registration process as shown in the last section. Such difference is determined by the underlying motivation of the two tasks. As stated in chapter one, the output of registration algorithm is a deformation field which will be further used for applications such as motion analysis and atlas segmentation, while the purpose of medical image interpolation is to increase the resolution perpendicular to the slice planes to restore the isotropy of the data set. So instead of the correspondence map, image interpolation algorithm generates the estimated

intermediate slices. Therefore, restrictions such as the smooth constraint may no longer be required for the purpose of interpolation and hence the idea of "interpolation lines" is more suitable for such circumstance rather than image warping process.

### 2.3.2 Interpolation Method

Figure 8 shows the outline of our interpolation method. Here we follow the idea of "interpolation lines" introduced in [47].

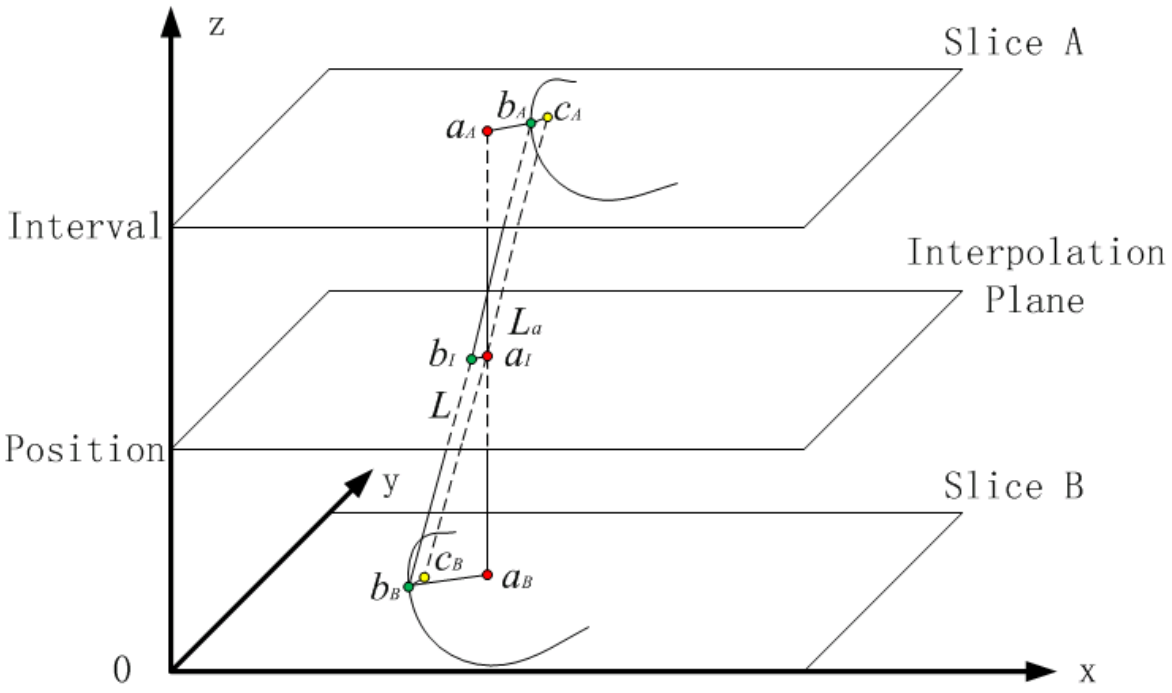


Figure 8 Illustration of computing the interpolation line $L$ associated with an image point $a_I$ on the interpolation plane with the information from t-scale in images of Slice A and Slice B.

To simplify the problem, we set a general coordinate system as shown above to avoid the three transformation matrices as stated in [47]. With this coordinate system, to calculate the intensity value at position $a_I = (i, j, \text{Position})$ on the interpolation plane,

the interpolation line $L$ is firstly generated from t-scale derived normal vectors $\overrightarrow{a_A b_A}$ and $\overrightarrow{a_B b_B}$. Record that normal vector at a point $p = (i, j, k)$ is $\boldsymbol{\tau}(p)$, we have $a_A = (i, j, Interval)$, $b_A = a_A + \boldsymbol{\tau}(a_A) = \big(i + \boldsymbol{\tau}_x(a_A), j + \boldsymbol{\tau}_y(a_A), Interval\big)$, $a_B = (i, j, 0)$, and $b_B = a_B + \boldsymbol{\tau}(a_B) = \big(i + \boldsymbol{\tau}_x(a_B), j + \boldsymbol{\tau}_y(a_B), 0\big)$. Further, $L$ is translated to $L_a$ so that it goes through position $a_I$. So $L_a$ can be written as:

$$\begin{bmatrix} x \\ y \\ z \end{bmatrix} = \begin{bmatrix} i \\ j \\ Position \end{bmatrix} + t \begin{bmatrix} \boldsymbol{\tau}_x(a_A) - \boldsymbol{\tau}_x(a_B) \\ \boldsymbol{\tau}_y(a_A) - \boldsymbol{\tau}_y(a_B) \\ Interval \end{bmatrix}$$

Then the intersections of $L_a$ with slices A and B, $c_A$ and $c_B$ are calculated respectively using the line function with two parameters $t_A = (Interval - Position)/Interval$ and $t_B = -Position/Interval$. The intensity values at $c_A$ and $c_B$ are calculated using bilinear interpolation on the two slice planes and intensity value at $a_I$ is finally calculated using linear interpolation between the intensity values at positions $c_A$ and $c_B$.

### 2.3.3 Local Scale and Medial Region Problem

In the implementation of t-scale based image interpolation, the unstable problem with region near the medial axis of a local structure, as mentioned in the registration section, is still a challenge. With the premise and character of t-scale based interpolation, this problem can be overcome by introducing another t-scale derived parameter "local scale", avoiding the information lost during smoothing process which is taken for registration. At any location $p$ in an image, local scale $LS(p)$ represents the scale of the local structure around $p$. By tracing t-scale thickness change along the opposite direction of the normal vector at $p$, the value of $LS(p)$ is determined by the local maxima of t-scale

thickness along the path. Figure 9 shows the local scale of a phantom image, it is obvious that the local scale at a location $p$ shows the size of local structure containing $p$.

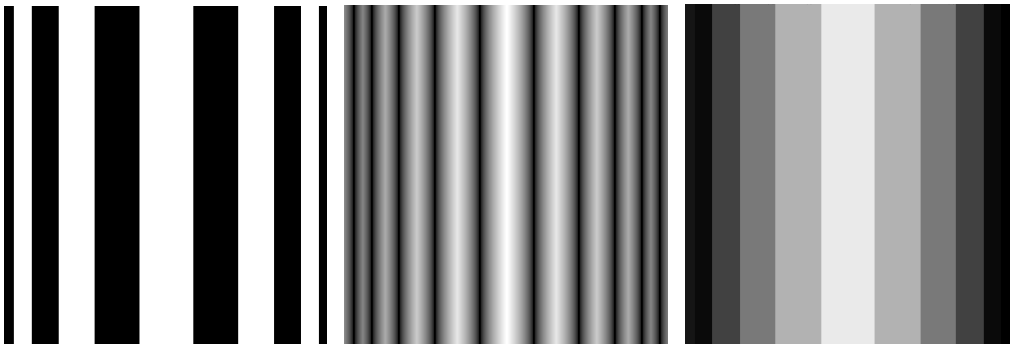

(a) (b) (c)

Figure 9 Local scale derived from t-scale used for image interpolation. (a) A binary phantom image with structures of different width. (b) Scale map (c) Local scale map with same value at locations contained in the structure of the same width.

With information provided by local scale and the assumption that the displacement of a structure between two adjacent slices should not be greater than half the structure size, the region near the medial axis of a structure can be identified and the unstable problem can be solved. Following the notations in Figure 8, as shown in Figure 10, let $k$ denotes the threshold defining the degree of adjacency, normal vectors $\boldsymbol{\tau}(a_A) = \overrightarrow{a_A b_A}$ and $\boldsymbol{\tau}(a_B) = \overrightarrow{a_B b_{B1}}$, if $|\boldsymbol{\tau}(a_A)| > k \cdot LS(a_A)$ or $|\boldsymbol{\tau}(a_B)| > k \cdot LS(a_B)$, then either of $a_A$ and $a_B$ are near the medial axis. Meanwhile, if the intensity value $|\mathrm{I}(a_A) - \mathrm{I}(a_B)| < threshold$, then $a_A$ and $a_B$ are within the same structure. Further, if the angle between $\boldsymbol{\tau}(a_A)$ and $\boldsymbol{\tau}(a_B)$ is greater than 90°, then an error is detected. Without losing generality, assuming $|\boldsymbol{\tau}(a_A)| < |\boldsymbol{\tau}(a_B)|$, then during interpolation line calculation, $\boldsymbol{\tau}'(a_B) =$

$\overrightarrow{a_B b_{B2}} = 2LS(a_B) - \boldsymbol{\tau}(a_B)$ is used instead of $\boldsymbol{\tau}(a_B)$. In this way, the interpolation line $L(a_I)$ can be correctly generated.

Also, in case there are some computation errors during t-scale computation, an outlier detection and correction process is further applied to the interpolation line set before the final interpolation result is generated. Considering a region $\Omega$ centered at a candidate point $p$, to determine if $L(p)$ is an outlier, a polynomial fit is applied to $L(a), a \in \Omega$. If $L(p)$ is far from the polynomial result at $p$, $L(p)$ is considered computation error and its value will be replaced by the polynomial result at $p$.

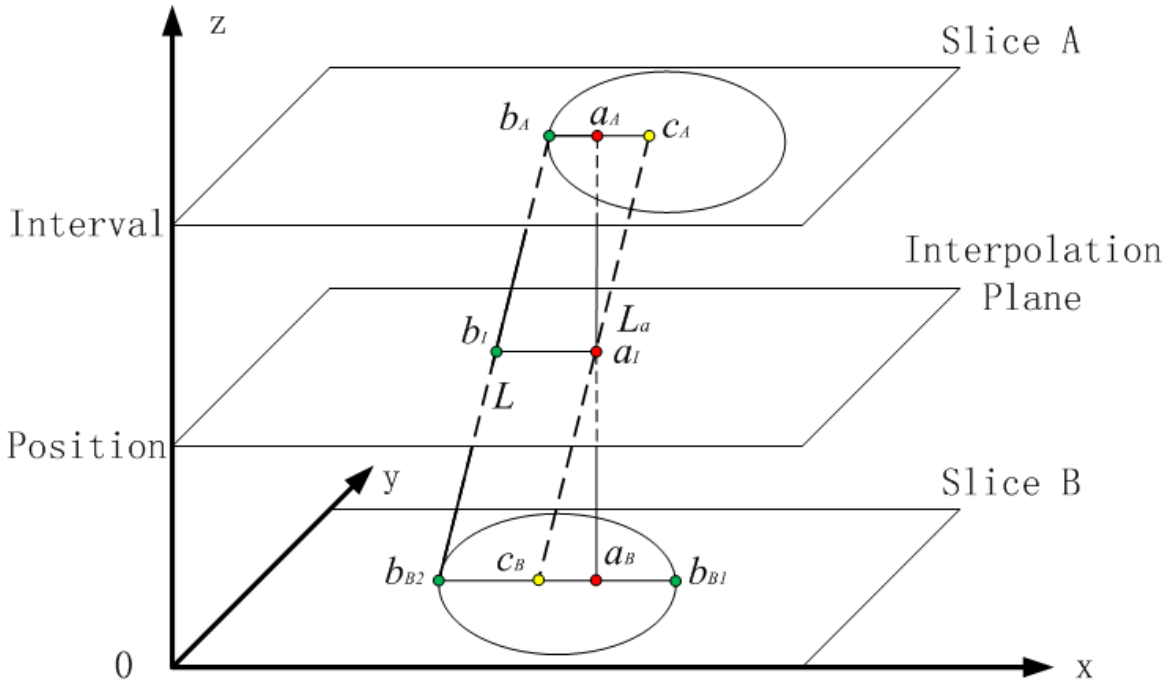


Figure 10 Illustration of correcting false coupled normal vectors near medial axis of a structure using local scale. The interpolation line $L$ is calculated using $\overrightarrow{a_B b_{B2}}$ instead of original normal vector $\overrightarrow{a_B b_{B1}}$.

### 2.3.4 Performance Evaluation

For a given 3D image consists of $k$ slices, each slice except the first and last slice is removed one at a time. The interpolation algorithm is then used to interpolate between its neighboring slices to produce an estimated version of the removed slice. The error is further evaluated between the interpolated slice and the corresponding removed slice using 2 error measures of mean absolute difference and mean square difference. Let $I_{int}(x, y, i)$ and $I_{rem}(x, y, i)$ respectively denote the intensity in slice $i$ at position $(x, y)$ in the interpolated and removed slice, the size of image is $m \times n \times k$, then the mean absolute difference is defined as

$$MAD = \frac{1}{k-2}\sum_{i=2}^{k-1}\frac{1}{m \cdot n}\sum_{x=1}^{m}\sum_{y=1}^{n}|I_{int}(x, y, i) - I_{rem}(x, y, i)|$$

The mean square difference is defined as

$$MSD = \frac{1}{k-2}\sum_{i=2}^{k-1}\frac{1}{m \cdot n}\sum_{x=1}^{m}\sum_{y=1}^{n}\left(I_{int}(x, y, i) - I_{rem}(x, y, i)\right)^2$$

# CHAPTER THREE

# RESULTS

## 3.1 T-scale based Registration

Here, we present preliminary results of application of the proposed t-scale based registration method on two dimensional geometric shapes as well as on CT images of a cadaveric ankle specimen. The performance of the method has been compared both qualitatively and quantitatively with that of a BSpline based method from ITK [55]. The method uses 4-level multi-resolution realization of BSpline deformable registration, applying mattes mutual information as metric, using regular step gradient decent optimizer, and setting grid size on image to 8.

### 3.1.1 Applications to Image Warping for Geometric Shapes

Figure 11 illustrates the result of application of the method to warping a disk (target shape) onto a square (reference shape). Results of deformation from Figure 11 (a) to Figure 11 (b) after application of t-scale based method for 10, 50 and 100 iterations are presented in Figure 11 (c, d, e), respectively. The result of deformation after applying the spline based method for 100 iterations is presented in Figure 11 (f). It is evident from Figure 11 (c, d, e) that the t-scale based method has been remarkably successful in producing the sharp corners of the square while deformed from the round shape of the disk. On the other hand, the BSpline based method has failed to show the same performance (with specific grid spacing and iteration times). Figure 12 illustrates intermediate results of warping from a Y-like shape to a disk via an intermediate shape shown in Figure 12 (e). As depicted in the figure, the method has been successful in blending both concave and convex corners into round shapes.

(a) (b) (c)

(d) (e) (f)

Figure 11 Illustration of warping a disk onto a square. (a, b) Original target and reference shapes. (c-e) Derived shapes after applying t-scale based warping method for 10, 50, 100 iterations, respectively. (f) The shape derived by applying the BSpline based warping method for 100 iterations.

(a) (b) (c) (d)

(e) (f) (g) (h)

Figure 12 Illustrations of different shapes during deformation of a Y-like target shape (a) onto a disk (h) via an intermediate shape (e) using the t-scale based method. Intermediate shapes during warping from (a) to (e) are shown in (b-d) while (f-g) illustrate intermediate shapes between (e) and (h).

### 3.1.2 Applications to 2D registration of CT images

The effectiveness of the method has been quantitatively examined on a CT image of a cadaveric ankle specimen. A cadaveric ankle specimen was scanned in a Siemens Sensation 64 Multi-slice CT scanner at 120 kVp and 140 mAs to adequately visualize the bony structures. After scanning in a helical mode with a slice thickness of 0.6 mm and collimation of 12×0.6 mm, data was reconstructed at 0.3 mm slice thickness with a normal cone beam method utilizing a very sharp algorithm of U75u to achieve high image resolution. Image parameters for these scans were as follows: matrix size =512×512 pixels; number of slices =314; pixel size =0.21mm. Two image slices from the CT scan are illustrated in Figure 13(a, b). The method was applied on 20 pairs of image slices randomly selected from the 3D CT image data set. Each pair consists of two successive image slices of which one is considered as the target image and the other as the reference one. The target image is deformed onto the reference image using the t-scale based method and the mean absolute error between the registered and the reference image is computed. The mean and standard deviation of average absolute initial errors (i.e., difference between original reference and target images) for 20 pairs and that after registration using t-scale and BSpline based methods are presented in Table 1. Table 1 demonstrates the t-scale based method reduces the original difference between the target and reference images and performs slightly better as compared to the BSpline based method in mean absolute errors. The reduction of absolute errors after t-scale based registration is also evident from Figure 13.

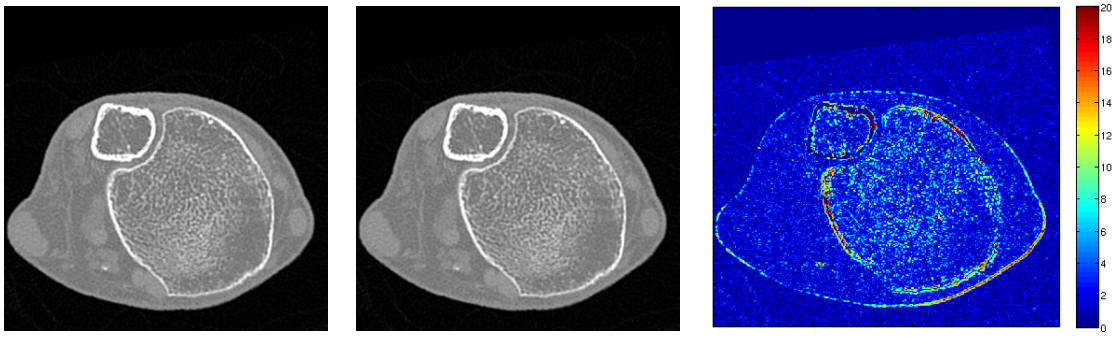


(a) (b) (c)

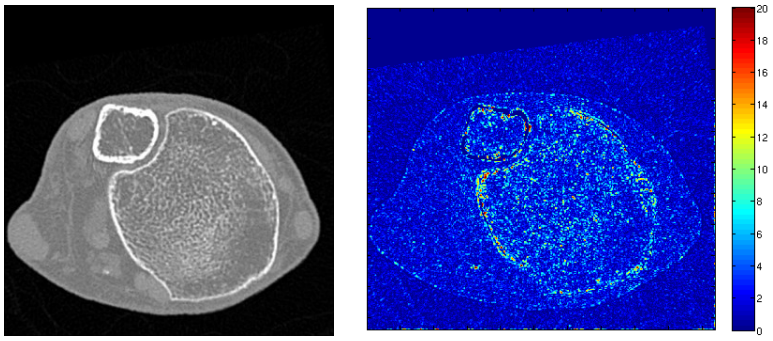


(d) (e)

Figure 13 Results of application of t-scale based image registration on two successive image slices from CT data set of a cadaveric ankle specimen. (a) Reference image. (b) Target image. (c) Absolute difference map between (a) and (b). (d) Result of registration of (b) onto (a) using t-scale method. (e) Same as (c) but between (a) and (d). It may be viewed that the reduction of error is clearly visible in (e).

Table 1 Mean absolute errors (gray value range 0~255) and standard deviation of the absolute errors between 20 pairs of successive image slices before and after applying different registration methods.

| | original | spline | tensor scale |
|---|---|---|---|
| mean absolute error | 2.95 | 2.64 | 2.57 |
| standard deviation | 3.52 | 2.97 | 3.03 |

## 3.2 T-scale based Interpolation

Here, we present preliminary results of application of the proposed t-scale based interpolation method on CT images. The performance of the method has been compared both qualitatively and quantitatively with that of registration based method [47]. Both BSpline based method and Demons method designed from ITK [55] are used for registration part.

### 3.2.1 Data and Method Description

We use both phantom data and real images to test our method. Simulated brain MRI data from *BrainWeb* is used as phantom data. Simulated T1 image for anatomical model of normal brain with 0% noise, 0% intensity non-uniformity and $1 \times 1 \times 1\text{mm}$ spacing is selected and in-plane grid size $181 \times 217$. In order to test the algorithm's robustness on different noise and intensity non-uniformity level, correlated noise and intensity non-uniformity is added manually. To add correlated noise to an image with grid size $m \times n$, 2D random numbers with size $m \times n$ following uniform distribution in range $[0\ A]$ is first generated and then smoothed by Gaussian filter to get an original noise image. To quantitatively measure the noise level, signal to noise ratio (SNR) is used. Let $A_{Image}\ (i,j)$ and $A_{Noise}\ (i,j)$ respectively denote the magnitude of image and noise at location $(i,j)$, we have original SNR in this case as

$$\text{SNR}_0 = \frac{\sum_{i=1}^{m}\sum_{j=1}^{n} A_{Image}^2\ (i,j)}{\sum_{i=1}^{m}\sum_{j=1}^{n} A_{Noise}^2\ (i,j)}$$

If we want to generate a noisy image $A_{NImage}\ (i,j)$ with $\text{SNR} = 100/\text{T}$, we need to scale the noise before add it to the original image as

$$A_{NIImage}\,(i,j) = A_{Image}\,(i,j) + A_{Noise}\,(i,j) \cdot \sqrt{\frac{\mathrm{SNR}_0}{\mathrm{SNR}}}$$

To add T% intensity non-uniformity, a Gaussian image is first generated with height $\max_{i\in[1,m],j\in[1,n]} A_{Image}\,(i,j) \cdot \mathrm{T}\%$, then added to the original image.

For real image, first group consists of 1 lung CT image with spacing $0.58 \times 0.58 \times 1.25\mathrm{mm}$, and 1 abdomen CT image with spacing $0.78 \times 0.78 \times 1\mathrm{mm}$ from *National Cancer Imaging Archive*, the in-plane grid size is reduced to $256 \times 256$; second group consists of 4 ankle CT images (left and right for 2 subjects) mentioned in the last section, the spacing is $0.21 \times 0.21 \times 0.3\mathrm{mm}$ and the in-plane grid size is reduced to $256 \times 256$; and the last group consists of 6 lung CT images (for 6 subjects) with spacing $0.55 \times 0.55 \times 0.5\mathrm{mm}$ and the in-plane grid size is reduced to $256 \times 256$. The reason we reduce the grid size is to save processing time for t-scale computation.

For comparison, registration based method is selected. The registration part is realized using both BSpline based algorithm as described in [47] and Demons algorithm [37]. Demons algorithm is chosen because it requires less parameters and yields more stable performance with much faster registration speed and better accuracy for some cases. For BSpline based registration algorithm, mean square metric and regular step gradient descent optimizer is applied. Following a multi resolution registration scheme, we design a 4-level registration method with grid size 16. The maximum step lengths are 16, 8, 4, 2, and the minimum step lengths are 1, 0.5, 0.1, 0.05. At each resolution level, if the minimum step length is reached or more than 1000 iterations occur, the algorithm moves to the next level. For demons method, we arbitrarily provide an iteration number

of 500, and from our observation, for most cases only minor change occurs in the updating metric value after 300 iterations.

### 3.2.2 Result on Phantom Data

Here, the results on *BrainWeb* phantom data generated by all 3 methods: t-scale based image interpolation, registration based image interpolation with BSpline, and registration based image interpolation with Demons are presented.

41 Slices are selected from the data and 39 results are generated for each method. Figure 14 shows the slice-by-slice mean absolute difference and Figure 15 shows square root of mean square difference for the data with image intensity range 0 to 65535.

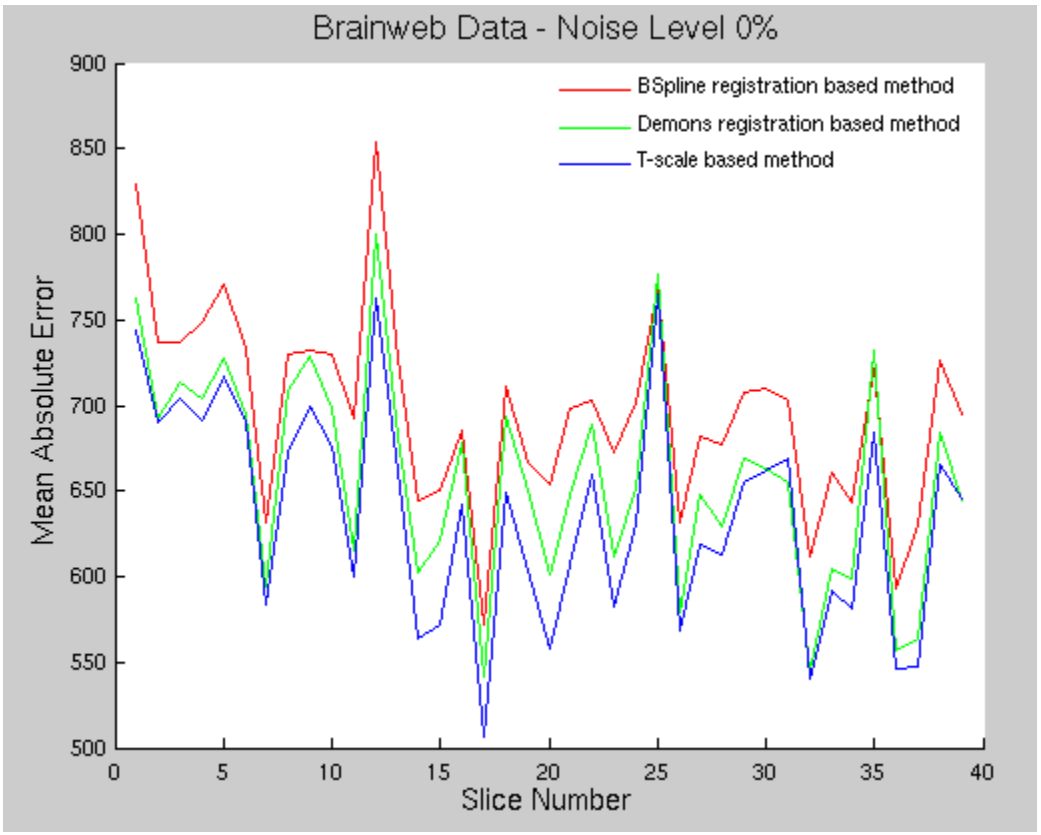


Figure 14 Performance of different interpolation methods on BrainWeb data at difference slices measured by MAD.

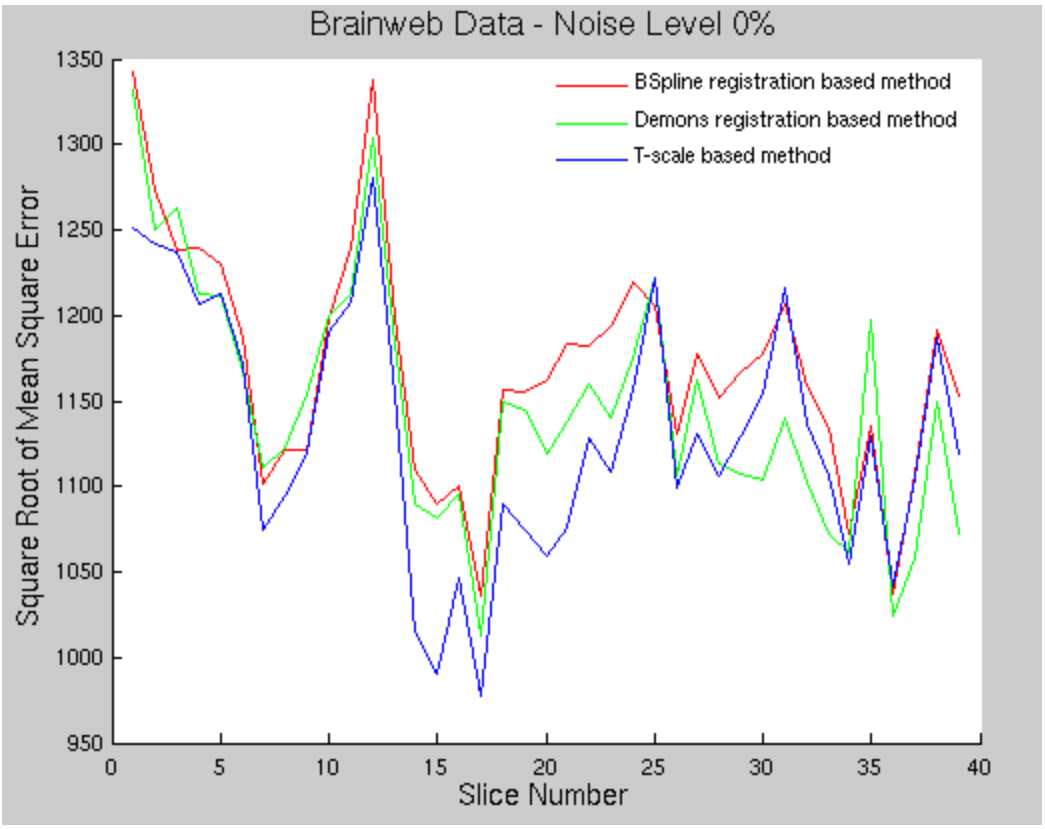


Figure 15 Performance of different interpolation methods on BrainWeb data at difference slices measured by square root of MSD.

It can be observed that t-scale based method outperforms the other two in sense of mean absolute difference and mean square difference at most of the slices. Paired t-test result is given in Table 2, as we can see, the results have statistical significance.

Table 2 Paired t-test result for slice-by-slice performance analysis

| t-test result | Demons & BSpline | Demons & T-scale | BSpline & T-scale |
|---|---|---|---|
| MAD | 1.3884E-14 | 1.64877E-10 | 5.91712E-21 |
| MSD | 1.98934E-05 | 0.0177143 | 8.62175E-09 |

Further, the robustness of the three methods is tested on different noise level and intensity non-uniformity level (sample shown in Appendix A). The result is shown in Figure 16 and Figure 17. The t-scale based method has a better and more stable performance.

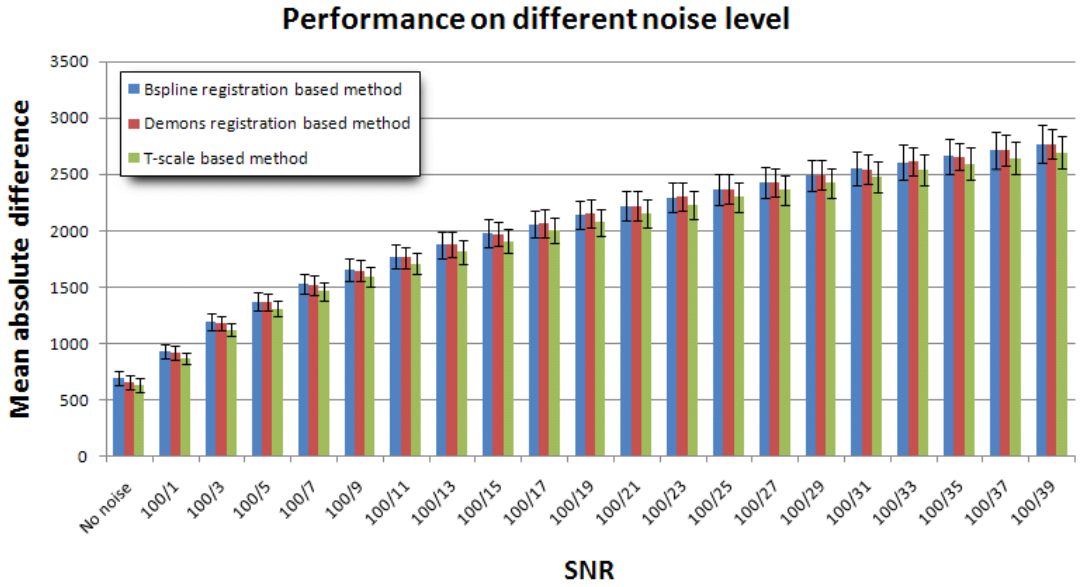


(a)

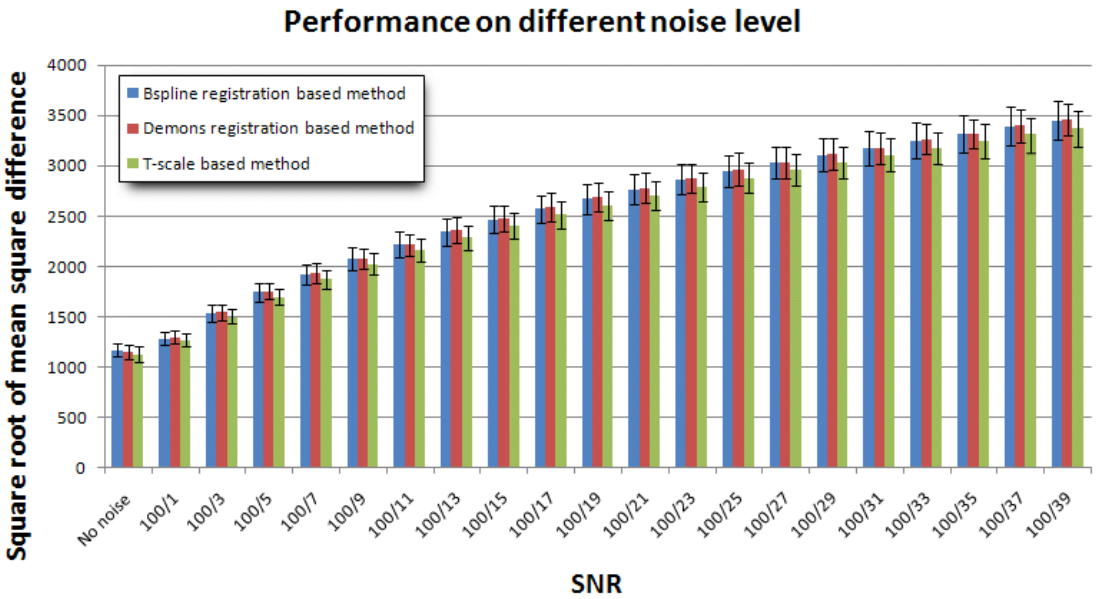


(b)

Figure 16 Performance of different methods for data at different noise level measured by (a) MAD and (b) square root of MSD.

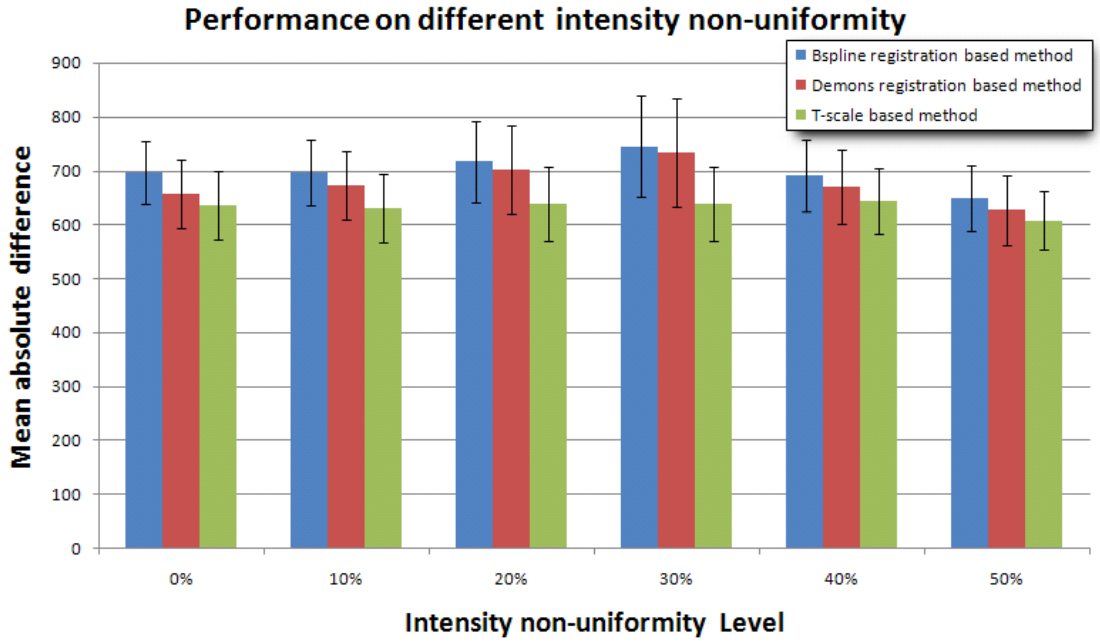


(a)

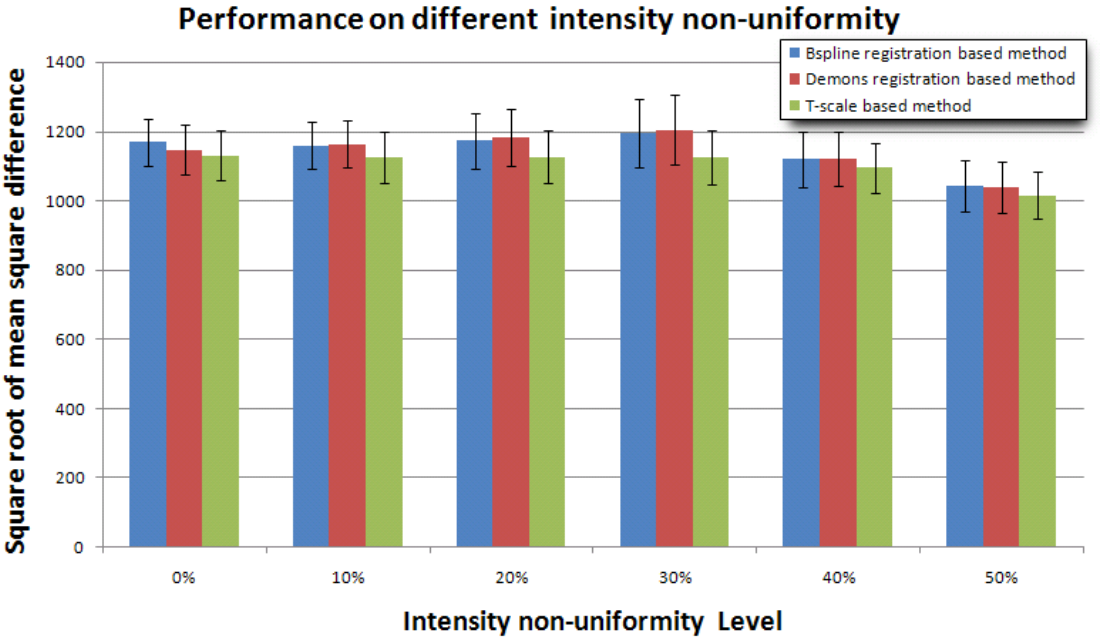


(b)

Figure 17 Performance of different methods for data at different intensity non-uniformity level measured by (a) MAD and (b) square root of MSD.

Paired t-test shows that for this experiment, the performance of t-scale based method has statistical significance compared with the other two.

### 3.2.3 Result on Real Image

The following gives the interpolation result on real images. 6 lung CT data: 001, 002, 031, 072, 084, 116; 4 ankle CT data: LT152, RT152, LT64, RT64; and tow NCIA data: lung and abdomen. For each image, 51 slices are selected.

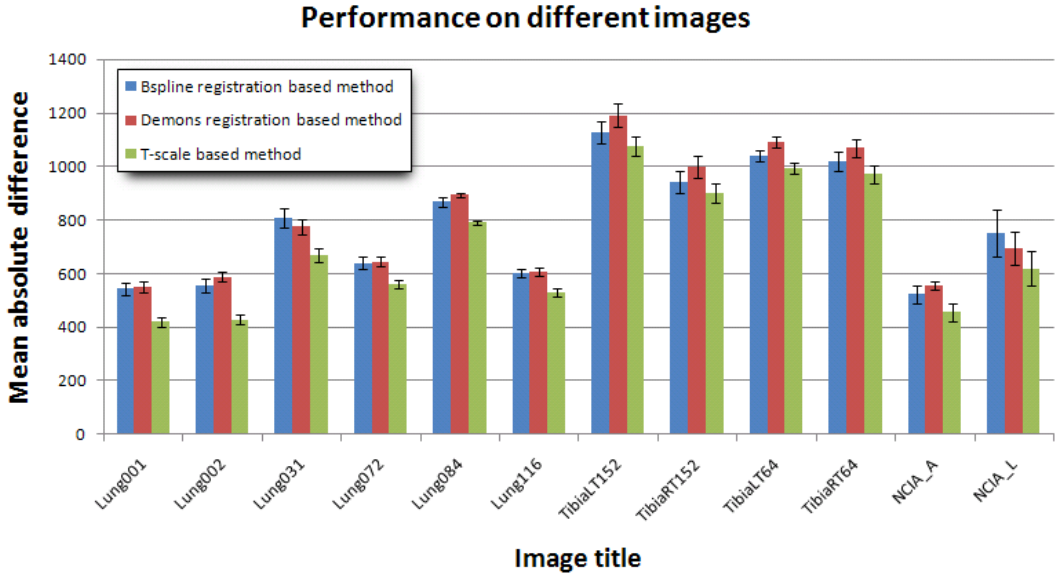


(a)

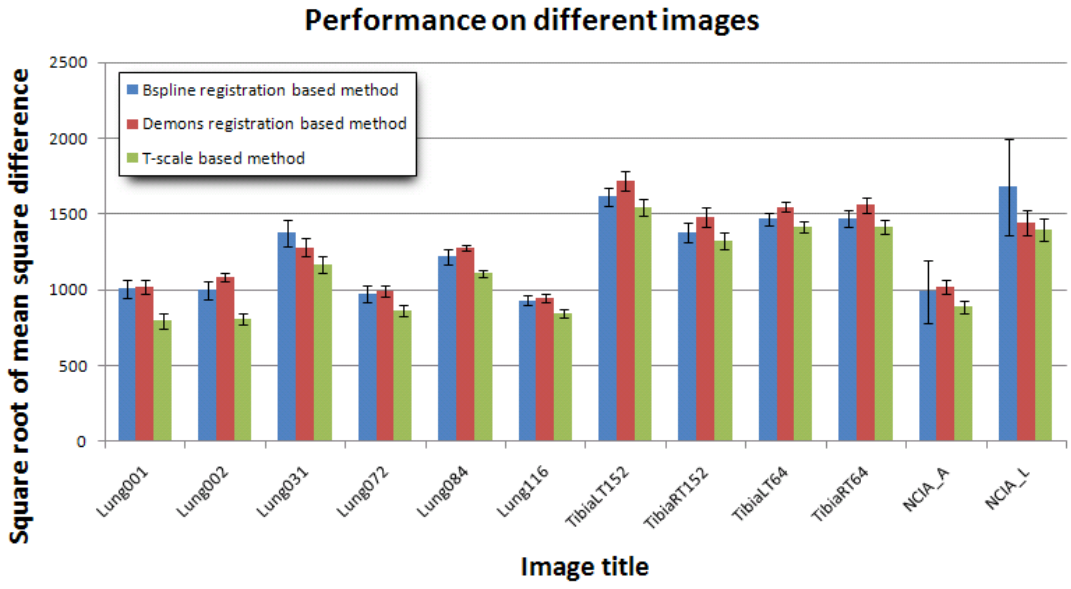


(b)

Figure 18 Performance of different methods on 12 images measured by (a) MAD and (b) square root of MSD.

As it can be observed from the result, for all images, t-scale based interpolation method outperforms the other two. Here we only present the overall performance of mean and standard deviation of the error measures for each image. Paired t-test shows that for this experiment, the performance of t-scale based method has statistical significance compared with the other two. Detailed slice-by-slice result and sample slices result are provided in Appendix B and C.

# CHAPTER FOUR

# DISCUSSION

In this project, most of the work is based on t-scale computation. Thus, the accuracy of t-scale is important. As many other image processing procedures, t-scale computation result is closely related to the selection of parameters of number of sample lines, length of sample lines, sigma of LoG, length of LoG, and threshold determining homogeneity. For different images, different selections are needed to ensure satisfying results, which will further influence the accuracy of registration and interpolation. Also for noisy images, we may need to apply pre-filtering to assist following t-scale computation. Therefore it will be necessary to investigate on parameter selection and pre-filtering in future research.

Currently, the implementation of t-scale based registration and interpolation are direct and definitive which require no optimization process. One problem with such implementation is that there are usually some errors that it cannot handle even we have considered all kinds of possibilities under our assumption. These errors may come from t-scale computation error in edge detection/ellipse fitting, or from the noise in the image. Therefore, we need to apply smooth filtering for registration and some correction for interpolation. In the future, we will develop a registration scheme that uses t-scale as a similarity measure following the traditional iterative non-rigid image registration framework.

# CHAPTER FIVE

# CONCLUSION

T-scale is a useful local morphometric parameter, and here, we have significantly improved the performance of the t-scale computation algorithm by enhancing edge detection and ellipse fitting algorithms. Further, we studied the application of t-scale in 2D image warping, registration and interpolation. Specifically, for registration, we have formulated a new t-scale derived feature called normal vector at each image point that denotes the vector joining the point to the nearest edge binding the local structure. This normal vector yields a more precise 360° orientation description of a local structure from the original 180° orientation information of t-scale. Normal vector is a useful image feature that can be directly computed from a gray level image requiring no image segmentation and it represents a high level morphological property in an image. A method has been developed based on it that directly computes the deformation field from a target image to a reference image. For interpolation, we have derived another t-scale based feature called local scale at each image point that represents the scale of the local structure around the point. Local scale is useful in determine if a point is near the medial axis of the local structure and thus is applied in correcting the errors generated by the direct computation process. The algorithms are tested on both phantom and real images and the performance is compared based on two error measures with other methods of BSpline based registration and registration based interpolation.

# APPENDIX A

## SAMPLE SLICES FOR ROBUSTNESS TEST

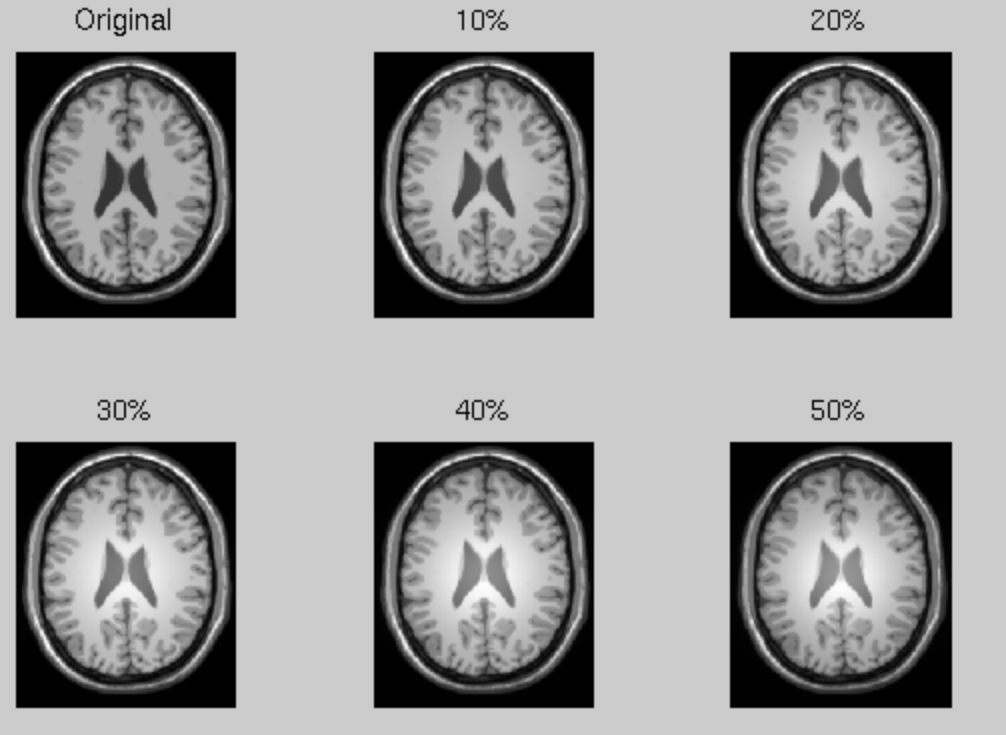


Figure A1 Phantom image for different level of intensity non-uniformity.

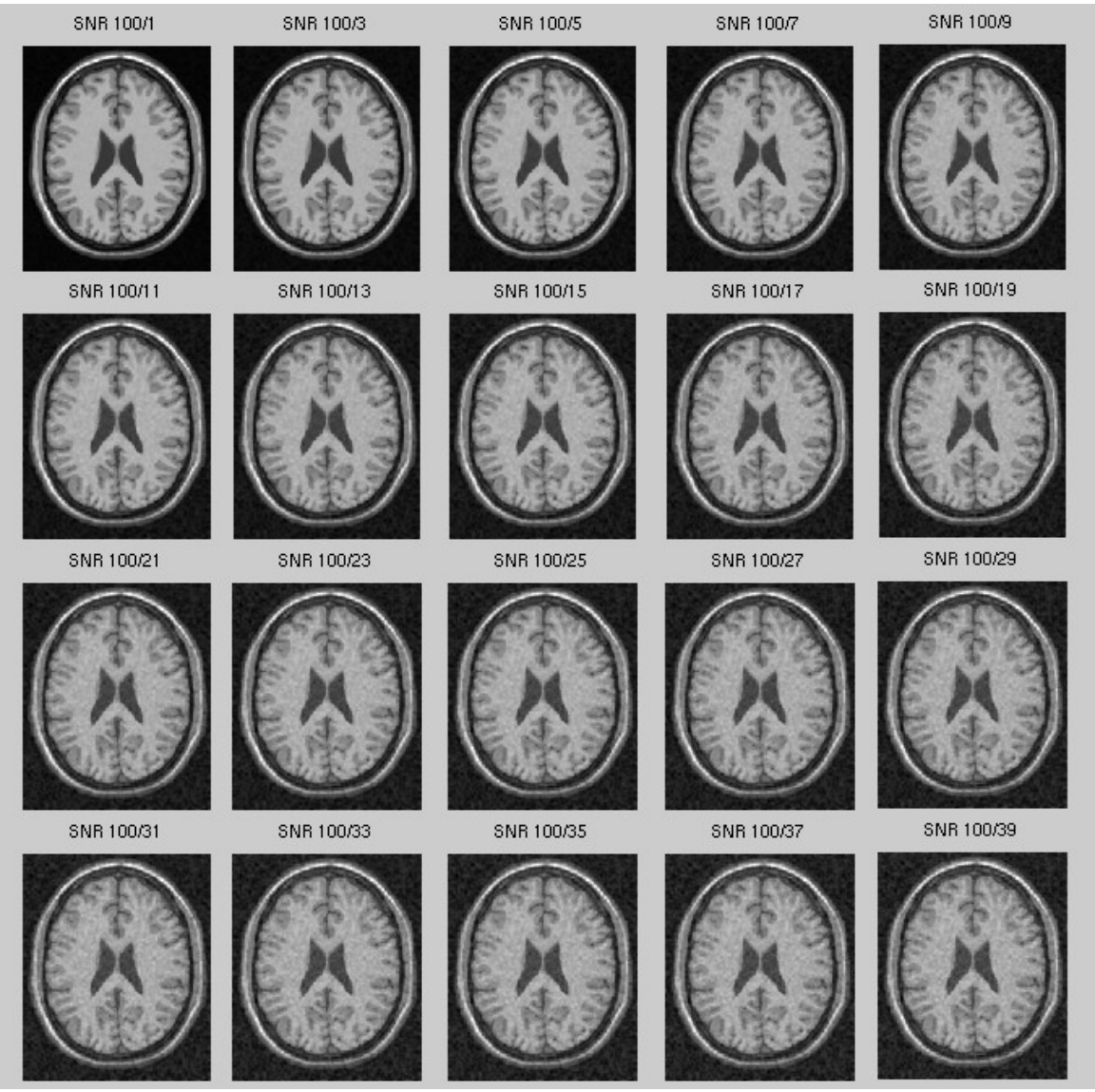


Figure A2 Phantom image for different noise level.

# APPENDIX B

## SLICE-BY-SLICE RESUTL FOR REAL DATA

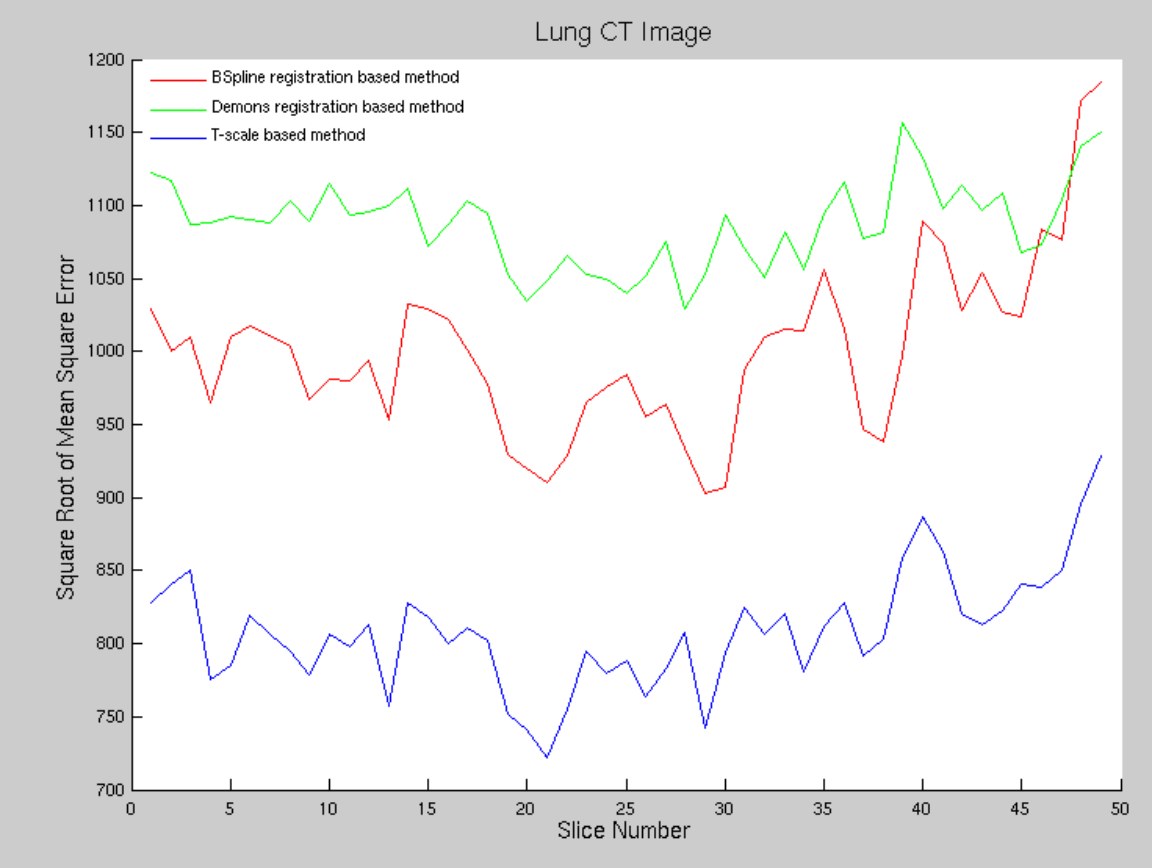


Figure B1 Slice-by-slice result of square root of mean square difference generated by 3 interpolation methods for lung CT data.

# APPENDIX C

## SAMPLE SLICES FOR REAL DATA

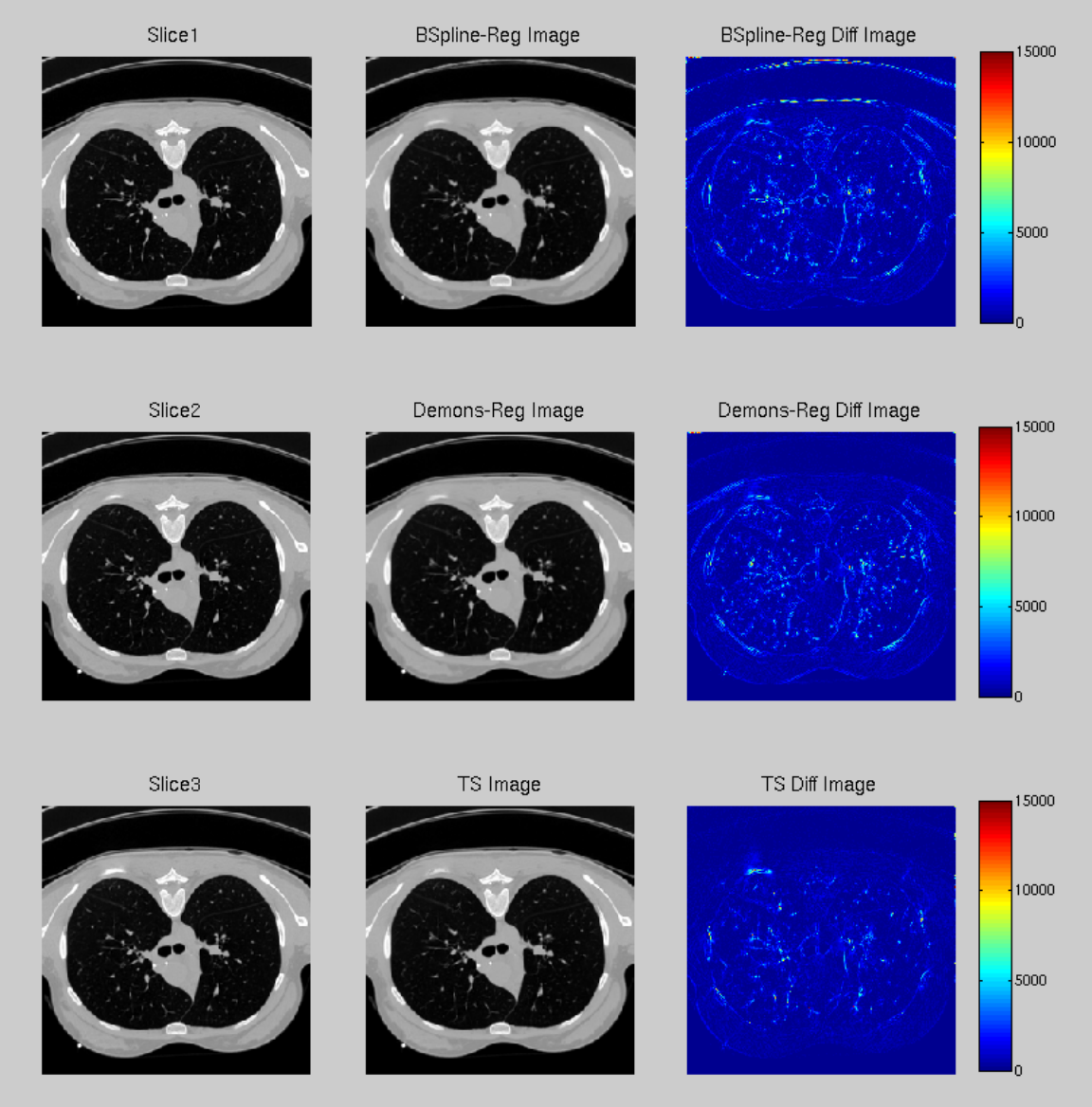


Figure C1 One sample slice from lung CT data with the result given by 3 different interpolation methods.

## REFERENCES


[1] D. Marr, *Vision*. San Francisco, CA: W. H. Freeman and Company, 1982.

[2] A. P. Witkin, "Scale-space filtering," presented at *8th International Joint Conference Artificial Intelligence*, Karlsruhe, West Germany, 1983.

[3] J. J. Koenderink, "The structure of images," *Biological Cybernatics*, vol. 50, pp. 363-370, 1984.

[4] T. Lindeberg, "Scale-space for discrete signals," *IEEE Transactions on Pattern Recognition and Machine Intelligence*, vol. 12, pp. 234-254, 1990.

[5] K. L. Vincken, A. S. E. Koster, and M. A. Viergever, "Probabilistic multiscale image segmentation," *IEEE Transactions on Pattern Analysis and Machine Intelligence*, vol. 19, pp. 109-120, 1997.

[6] Y. Leung, J. S. Zhang, and Z. B. Xu, "Clustering by scale space filtering," *IEEE Transactions on Pattern Analysis and Machine Intelligence*, vol. 22, pp. 1396-1410, 2000.

[7] B. C. Lovell and A. P. Bradley, "The multiscale classifier," *IEEE Transactions on Pattern Analysis and Machine Intelligence*, vol. 18, pp. 124-137, 1996.

[8] M. Ferraro, G. Bocclgnone, and T. Caell, "On the representation of image structures via scale space entropy conditions," *IEEE Transactions on Pattern Analysis and Machine Intelligence*, vol. 21, pp. 1190-1203, 1999.

[9] M. Tabb and N. Ahuja, "Multiscale image segmentation by integrated edge and region detection," *IEEE Transactions on Image Processing*, vol. 6, pp. 642-655, 1997.

[10] S. M. Pizer, D. Eberly, and D. S. Fritsch, "Zoom-invariant vision of figural shape: the mathematics of core," *Computer Vision and Image Understanding*, vol. 69, pp. 55-71, 1998.

[11] J. H. Elder and S. W. Zucker, "Local scale control for edge detection and blur estimation," *IEEE Transactions on Pattern Analysis and Machine Intelligence*, vol. 20, pp. 699-716, 1998.

[12] P. Liang and Y. F. Wang, "Local scale controlled anisotropic diffusion with local noise estimate for image smoothing and edge detection," presented at *International Conference in Computer Vision*, Bombay, India, 1998.

[13] P. K. Saha, J. K. Udupa, and D. Odhner, "Scale-based fuzzy connected image segmentation: theory, algorithms, and validation," *Computer Vision and Image Understanding*, vol. 77, pp. 145-174, 2000.

[14] P. K. Saha and J. K. Udupa, "Scale based image filtering preserving boundary sharpness and fine structures," *IEEE Transactions on Medical Imaging*, vol. 20, pp. 1140-1155, 2001.

[15] Y. Jin, A. F. Laine, and C. Imielinska, "Adaptive speed term based on homogeneity for level-set segmentation," presented at *SPIE: Medical Imaging*, San Diego, CA, 2002.

[16] Y. Zhuge, J. K. Udupa, and P. K. Saha, "Vectorial scale-based fuzzy connected image segmentation," presented at *SPIE: Medical Imaging*, San Diego, CA, 2002.

[17] L. Nyúl, J. K. Udupa, and P. K. Saha, "Task specific comparison of 3D image registration methods," presented at *SPIE: Medical Imaging*, San Diego, CA, 2001.

[18] A. D. A. Souza, J. K. Udupa, and P. K. Saha, "Volume rendering in the presence of partial volume effects," *IEEE Transactions on Medical Imaging*, vol. 24, pp. 223-235, 2005.

[19] P. K. Saha, "Novel theory and methods for tensor scale: a local morphometric parameter," presented at *SPIE: Medical Imaging*, San Diego, CA, 2003.

[20] P. K. Saha, "Tensor scale: a local morphometric parameter with applications to computer vision and image processing," *Computer Vision and Image Understanding*, vol. 99, pp. 384-413, 2005.

[21] M. Kass and A. Witkin, "Analyzing oriented patterns," *Computer Vision Graphics and Image Processing*, vol. 37, pp. 362-385, 1987.

[22] S. d. Zeno, "A note on the gradient of a multi-image," *Computer Vision Graphics and Image Processing*, vol. 33, pp. 166-125, 1986.

[23] H. Knutsson, "Representing local structures using tensors," presented at 6th *Scandinavian Conference on Image Analysis*, Oulu, Finland, 1989.

[24] J. v. d. Weijer, L. J. v. Vliet, P. W. Verbeek, and M. v. Ginkel, "Curvature estimation in oriented patters using curvilinear models applied to gradient vectoir fields," *IEEE Transactions on Pattern Analysis and Machine Intelligence*, vol. 23, pp. 1035-1043, 2002.

[25] B. Rieger and L. J. v. Vliet, "Curvature of n-dimensional space curve in grey-value images," *IEEE Transactions on Image Processing*, vol. 11, pp. 738-745, 2002.

[26] A. Madabhushi, J. K. Udupa, and A. Souza, "Generalized scale: theory, algorithms, and application to image inhomogeneity correction," *Computer Vision and Image Understanding*, vol. 101, pp. 100-121, 2006.

[27] P. K. Saha and J. K. Udupa, "Tensor scale-based fuzzy connectedness image segmentation," presented at *SPIE: Medical Imaging*, San Diego, CA, 2003.

[28] P. K. Saha, J. C. Gee, Z. Xie, and J. K. Udupa, "Tensor scale-based image registration," presented at *SPIE: Medical Imaging*, San Diego, CA, 2003.

[29] P. K. Saha and F. W. Wehrli, "A robust method for measuring trabecular bone orientation anisotropy at in vivo resolution using tensor scale," *Pattern Recognition*, vol. 37, pp. 1935-1944, 2004.

[30] P. K. Saha and F. W. Wehrli, "In vivo assessment of trabecular bone architecture via three-dimensional tensor scale," presented at *SPIE: Medical Imaging*, San Diego, CA, 2004.

[31] F. A. Andalo, P. A. V. Miranda, R. d. S. Torres, and A. X. Falcao, "A new shape descriptor based on tensor scale," presented at the 8th *International Symposium on Mathematical Morphology*, Rio de Janeiro, Brazil, 2007.

[32] F. A. Andalo, P. A. V. Miranda, R. d. S. Torres, and A. X. Falcao, "Detecting contour saliences using tensor scale," presented at *IEEE International Conference on Image Processing*, 2007.

[33] F. Ino, Y. Tanaka, K. Hagihara, and H. Kitaoka, "Performance study of nonrigid registration algorithm for investigating lung disease on clusters," presented at the *Sixth International Conference on Parallel and Distributed Computing Applications and Technologies*, 2005.

[34] J. Pettersson, H. Knutsson, and M. Borga, "Automatic hip bone segmentation using non-rigid registration," presented at *IEEE International Conference on Pattern Recognition*, 2006.

[35] D. Rueckert, L. I. Sonoda, C. Hayes, D. L. Hill, M. O. Leach, and D. J. Hawkes, "Nonrigid registration using free-form deformations: application to breast MR images," *IEEE Transactions on Medical Imaging*, vol. 18, pp. 712-721, 1999.

[36] K. Rohr, H. S. Stiehl, R. Sprengel, T. M. Buzug, J. Weese, and M. H. Kuhn, "Landmark-based elastic registration using approximating thin-plate splines," *IEEE Transactions on Medical Imaging*, vol. 20, pp. 526-534, 2001.

[37] J. P. Thirion, "Image matching as a diffusion process: an analogy with Maxwell's demons," *Medical Image Analysis*, vol. 2, pp. 243-260, 1998.

[38] W. M. Wells-III, P. Viola, H. Atsumi, S. Nakajuma, and R. Kikinis, "Multi-modal volume registration by maximization of mutual information," *Medical Image Analysis*, vol. 1, pp. 35-51, 1996.

[39] R. Bajcsy and S. Kovacic, "Multiresolution elastic matching," *Computer Vision Graphics and Image Processing*, vol. 46, pp. 1-21, 1989.

[40] M. Bro-Nielsen and C. Gramkow, "Fast fluid registration of medical images," presented at *Visualization in Biomedical Computing*, Hamburg, Germany, 1996.

[41] G. E. Christensen, R. D. Rabbitt, and M. I. Miller, "Deformable templates using large deformation kinematics," *IEEE Transactions on Image Processing*, vol. 5, pp. 1435-1447, 1996.

[42] P. Rogelj and S. Kovacic, "Similarity measures for non-rigid registration," presented at *SPIE Medical Imaging* 2001: Image Processing, 2001.

[43] G.J. Grevera and J.K. Udupa, "An objective comparison of 3-D image interpolation methods," *IEEE Transactions on Medical Imaging*, vol. 17, pp. 642-652, 1998.

[44] P. Thevenaz, T. Blu, and M. Unser, "Interpolation revisited," *IEEE Transactions on Medical Imaging*, 2000

[45] G.T. Herman, J. Zheng, and C.A. Bucholtz, "Shape-based interpolation," *IEEE Computer Graphics and Application*s, vol.12, pp. 69-79, 1992.

[46] S.P. Raya and J.K. Udupa, "Shape-based interpolation of multidimensional objects," *IEEE Transactions on Medical Imaging*, vol. 9(5), pp. 32-42, 1990.

[47] G.P. Penny, J.A. Schnable, D. Rueckert, M.A. Viergever, and W.J.Niessen, "Registration-based interpolation," *IEEE Transactions on Medical Imaging*, vol.23(7), pp.922-926, 2004.

[48] T. Y. Lee and W.H. Wang, "Morphology-based three-dimensional interpolation," *IEEE Transactions on Medical Imaging*, vol. 19, pp. 711-721, 2000.

[49] M. Sonka, V. Hlavac, and R. Boyle, *Image Processing, Analysis, and Machine Vision*. Pacific Grove, CA: PWS Publishing, 1999.

[50] S. R. Gunn, "On the discrete representation of the laplacian of gaussian," *Pattern Recognition*, vol. 32, pp. 1463-1472, 1999.

[51] A. Fitzgibbon, M. Pilu, and R. B. Fisher, "Direct least square fitting of ellipses," *IEEE Transactions on Pattern Analysis and Machine Intelligence*, vol. 21, pp. 476-480, 1999.

[52] F. L. Bookstein, "Fitting conic sections to scattered data," *Computer Graphics and Image Processing*, vol. 9, pp. 56-71, 1979.

[53] P. L. Rosin, "A note on the least squares fitting of ellipses," *Pattern Recognition Letters*, vol. 14, pp. 799-808, 1993.

[54] G. E. Christensen and H. J. Johnson, "Consistent Image Registration," *IEEE Transactions on Medical Imaging*, vol. 20, 2001

[55] Luis Ibanez and William Schroeder *The ITK Software Guide*. Kitware, Inc. 2005.